The geomagnetic field intensity in New Zealand: palaeointensities from Holocene lava flows of the Tongariro Volcanic Centre

Annika Greve,[1,2] Mimi J. Hill,[3] Gillian M. Turner[2] and Andreas Nilsson[4]

[1]*School of Geography, Environment and Earth Sciences, Victoria University of Wellington, P.O. Box 600, Wellington 6140, New Zealand.*
E-mail: Annika.Greve@vuw.ac.nz
[2]*School of Chemical and Physical Sciences, Victoria University of Wellington, P.O. Box 600, Wellington 6140, New Zealand*
[3]*Geomagnetism Laboratory, School of Environmental Sciences, University of Liverpool, Liverpool L69 7ZE, United Kingdom*
[4]*Department of Geology, Lund University, Sölvegatan 12, 223 62 Lund, Sweden*

SUMMARY

Very few absolute palaeointensity data exist from Holocene-aged rocks in New Zealand. Here we present a new suite of high-quality palaeointensities, supported by detailed rock magnetic investigations. Samples from 23 sites representing 10 distinct eruptive units of the Tongariro Volcanic Centre, Taupo Volcanic Zone, New Zealand, were studied. Both traditional double heating and microwave palaeointensity methods were employed. The reliability of the palaeointensity data varies with rock magnetic properties of the samples, corresponding, in particular, to their positions within the lava flows. The highest success rates are from samples obtained from near the flow tops where a significant proportion of the remanence unblocked at intermediate temperatures (200–350 °C). By contrast, samples from flow centres, particularly the parts showing platey fracturing, have the lowest success rates. Reliable, high-quality palaeointensity results ranging from 32.4 ± 5.1 µT to 72.1 ± 4.7 µT were obtained from six flows with ages between c. 12 800 yr BP and the present. These correspond to virtual dipole moments that increase from 52 ± 10 ZAm^2 in the early Holocene and peak at 112 ± 14 ZAm^2 about 300 yr ago. The data agree well with calibrated relative palaeointensities from New Zealand lake sediments. The volcanic and sedimentary data together yield a Holocene virtual axial dipole moment curve that fits the global average variation well in the early Holocene, but which differs significantly in recent millennia. This difference is associated with recent migration of the southern high latitude core–mantle boundary flux lobe towards New Zealand, as is seen in global field models.

Key words: New Zealand; Magnetic mineralogy and petrology; Palaeointensity; Palaeomagnetic secular variation.

1 INTRODUCTION

The thermoremanent magnetization (TRM) acquired by lava flows during cooling provides a unique opportunity of obtaining instantaneous and absolute records of geomagnetic palaeointensity beyond times of direct observation. Compilations of intensity records give estimates of variations in Earth's dipole moment throughout time and thus yield important information about the dynamics of Earth's core (e.g. Olson 2002). In order to obtain a reliable record of the global dipole moment, well distributed datasets are required. The detrital remanent magnetization recorded by lacustrine and marine sediments, on the other hand, provide continuous smoothed records of Earth's magnetic field through time. They are often well-dated, and existing sedimentary records have a better global coverage than volcanic datasets, making them particularly valuable for integration into models of field variation through time. However, they provide relative palaeointensity data only and rely on calibration to absolute values obtained from other sources, such as volcanic materials.

Global models of Earth's magnetic field (e.g. Nilsson *et al.* 2014; Pavón-Carrasco *et al.* 2014; Constable *et al.* 2016) are based disproportionately on absolute palaeointensity data from the northern hemisphere. Further, data quality is strongly affected by differences in the sampling and experimental procedures, the criteria used to select 'successful' data (e.g. Donadini *et al.* 2006; Knudsen *et al.* 2008) and limitations in the age constraints provided (e.g. Greve & Turner 2017). The stepwise double-heating palaeointensity method has grown from the pioneering work of Koenigsberger (1938) and Thellier & Thellier (1959), and its modifications are still considered by many to be the most reliable method of estimating absolute palaeointensities from natural TRM-bearing materials (Selkin & Tauxe 2000). It is based on the assumption of a linear relationship between a natural TRM and a laboratory-induced TRM. In practice the NRM is replaced stepwise by a laboratory-induced partial TRM (pTRM) while exposing the samples to higher temperature with each step. For the linear relation to be valid, the primary remanence carrier should be of single domain (SD) size (e.g. Levi 1977;

Riisager & Riisager 2001) and of a thermally stable composition so that the ability to obtain a TRM does not change during an experiment. Neither of these requirements is easy to satisfy. First, the grain sizes found throughout subaerial lava flows are usually within the pseudo-single domain (PSD) or multidomain (MD) grain range (Dunlop & Özdemir 1997). Second, the main remanence carriers in intermediate composition lava flows usually belong to the Fe–Ti-oxide ternary system, which includes titanomagnetites and their oxidation products. Within this system equilibrium temperatures and oxygen fugacities control the compositions of co-existing spinel [magnetite (mt)—ulvöspinel (ulv)] and orthorhombic [hematite (hem)-ilmenite (ilm)] phases (e.g. Sauerzapf *et al.* 2008). Rapid cooling or quenching of lava often results in the formation of solid solutions that are metastable at low temperature, and that evolve towards equilibrium composition when reheated during palaeointensity or thermomagnetic experiments. Such alteration affects a sample's ability to carry TRM and can therefore result in significant error in the palaeointensity calculation. The microwave technique (Hill & Shaw 2000; Suttie *et al.* 2010) was designed to minimize alteration by exciting the magnetic moments of the ferro-/ferrimagnetic grains using energetic microwaves instead of a heating procedure, while otherwise using a procedure similar to that used for thermal palaeointensity determination.

In this paper we present the results of detailed magneto-mineralogical and palaeointensity studies using both traditional Thellier-type double heating and microwave palaeointensity methods, on intermediate composition lavas younger than 15 ka from Ruapehu and Tongariro volcanoes in the central North Island, New Zealand. Similarities in the overall mineralogy of individual flows and sampling throughout their thickness allows us to draw conclusions regarding the suitability of different zones within the lava flows for palaeointensity determination as well as providing much needed Southern Hemisphere palaeointensity data.

2 SAMPLES

The Tongariro Volcanic Centre (TgVC) is a complex of several andesitic to dacitic composite volcanoes, located at the southern extremity of the Taupo Volcanic Zone, with effusive activity extending back at least 350 kyr (Tost & Cronin 2015) and lasting into recent centuries (e.g. Hobden *et al.* 1996; Gamble *et al.* 2003; Eaves *et al.* 2015; Conway *et al.* 2016; Greve *et al.* 2016). Holocene eruptive activity around Ruapehu volcano was dominated by a voluminous pulse of activity lasting more than 1000 yr following a major sector collapse event at c. 10.5 ka (Eaves *et al.* 2015; Conway *et al.* 2016), while only a few effusive lava producing eruptions have occurred since 5 ky BP. In contrast, around Mt Tongariro, effusive activity has occurred throughout the past few centuries (Hobden *et al.* 1996, 2002; Hobden 1997; Greve *et al.* 2016).

The palaeosecular variation study described in Greve *et al.* (2016) involved detailed sampling of 12 post-glacial andesitic flows or flow packages from the TgVC of which 11 were located around Ruapehu volcano. The sampling was carried out in conjunction with a geological mapping programme on Ruapehu volcano (Townsend *et al.*, in preparation; Fig. 1). In this paper we describe palaeointensity experiments on ten units for which palaeomagnetic directions were previously obtained (Fig. 1; Greve *et al.* 2016). Each flow is known to be of post-glacial age (<15 ka) due to its position within glacial moraines and millennial scale age-control from ^{40}Ar/^{39}Ar data (Conway *et al.* 2016) or tephra bracketing. Greve *et al.* (2016) further refined these ages by matching the individ-

ual palaeomagnetic directions with the continuous palaeosecular variation (PSV) record of Turner *et al.* (2015), for which a high-resolution, radiocarbon based age model is available. Descriptions of the individual flows are summarized in Table 1. Full sampling details and directional results are described in Greve *et al.* (2016).

The morphology and exposure of the individual flows varies widely (Table 1). Similarities were however identified between the fracture patterns of the generally thick (>5 m) andesitic flows around Mt Ruapehu which we subdivide into four zones (Fig. 2). Zone A is the basal part, which is not often exposed; zone B corresponds to the flow centre, which is characterized by strong sub-horizontal, platey fracturing, produced during cooling. This is overlain by the blocky and often vertically jointed zone C. Where not eroded, the flows are capped by strongly auto-brecciated or a'a flow tops (zone D). Where possible, lava flows were sampled at multiple sites along their length and through their thickness. A full sequence through all four zones was exposed and sampled only at one locality (WE flow, Table 1).

Collection of drilled samples was often hindered by the hardness of the andesites, and so additional hand samples were collected. These were usually removed from the outcrop after marking the strike and dip on an exposed flat surface, and later drilled with a vertical drill-press in the laboratory. Flat surfaces were not easy to find on the brecciated surface of a'a flow top and some hand samples were either poorly oriented or un-oriented. While such samples were not included in the directional study of Greve *et al.* (2016), some were used for palaeointensity experiments and, in Table 3, their results are marked accordingly.

3 MAGNETIC MINERALOGY AND ROCK MAGNETISM

3.1 Methods

Mineral-optical investigations, including transmitted and reflected light microscopy and electron microprobing were conducted at the School of Geography, Environment and Earth Sciences at Victoria University of Wellington. Polished thin sections were coated with a thin carbon film prior to electron microprobe analysis. Petrographic imaging was carried out using an *Olympus* BX51 research microscope with a maximum magnification of 400x. Backscatter electron (BSE) imaging and wavelength dispersive x-ray spectroscopy (WDX) were conducted on a selection of samples using a *JEOL* JXA-8230 scanning electron microprobe.

Detailed rock magnetic experiments were conducted at the palaeomagnetism laboratory at the University of Liverpool. A Variable Field Translation Balance (VFTB) was used for successive measurement of isothermal remanent magnetization (IRM) acquisition, backfield coercivity of remanence, hysteresis and variation of saturation magnetization with temperature (M_s versus T) using a peak field of 800 mT and to a peak temperature of 700 °C in ambient atmosphere. Low-field magnetic susceptibility (χ versus T) was measured in an inert argon environment, cycling the samples from room temperature to a peak temperature of 700 °C and back, using an *AGICO* MFK1-FA Kappa Bridge.

3.2 Petrographic description, microscopy and BSE imaging

All Ruapehu lava flows targeted in this study share similarities in composition (Price *et al.* 2012; Conway *et al.* 2016) and rock
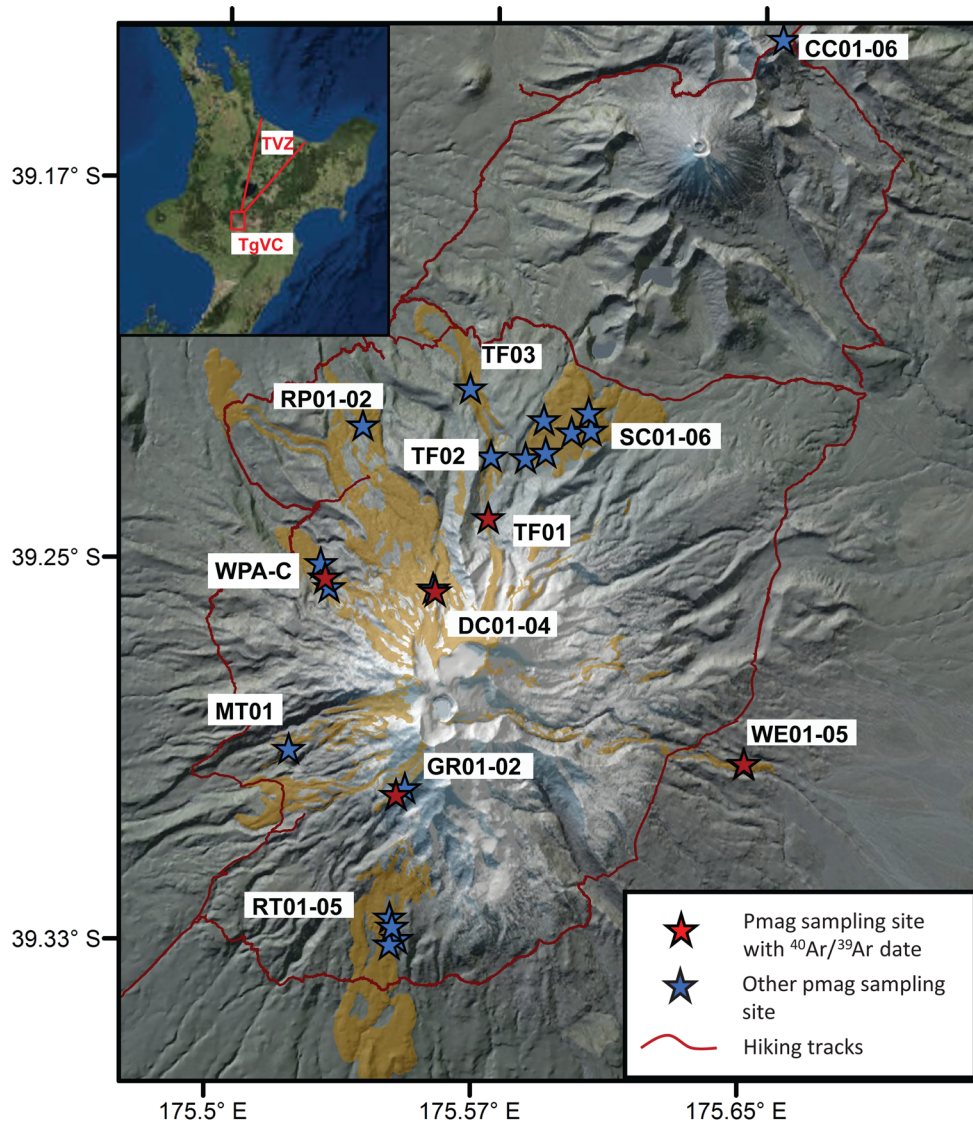
Figure 1. Digital topographic map of Ruapehu Volcano in the Tongariro Volcanic Centre (after Greve *et al.* 2016). Approximately 12 km north of Ruapehu, and 3 km southwest of site CC is the young cone of Mt Ngauruhoe, and about 3 km north of this the summit of Tongariro. Approximately 15 km further north are the peaks of Pihanga and Kakaramea, which are also considered part of the TgVC. The postglacial lava flows on Mt Ruapehu (Whakapapa Formation) are shaded brown. Palaeomagnetic sampling sites of Greve *et al.* (2016) are shown as stars: sites for which ^{40}Ar/^{39}Ar ages are available are shown in red, others in blue. The initial two letters of the site names denote the flow or sequence of flows. No palaeointensity experiments were conducted on Saddle Cone (SC) flows. Inset: location of the TgVC at the southern tip of the Taupo Volcanic Zone (TVZ) in the North Island, New Zealand. Base map information from Land Information New Zealand (LINZ).

magnetic behaviour. Central Crater (CC) flow is the only unit sampled from a different cone, Red Crater. It is of more mafic composition and different morphology (Table 1). CC samples are basaltic andesites [Phenocrysts: plagioclase (plag), orthopyroxene (opx), clinopyroxene (cpx), olivine (ol) and isolated oxides at the submicron scale]. They contain a quenched glassy matrix with isolated brown glass with c. 30 per cent vesicle space (flow-top samples; e.g. sample CC06A, Fig. 3a). The samples from the Ruapehu flows are porphyritic andesites with a phenocryst (mainly plag, some opx and cpx) abundance of 30–50 per cent in a microcrystalline matrix consisting of mostly elongated plagioclase grains [e.g. Mangaturuturu (MT) flow sample MT05A Fig. 3b]. Fe–Ti oxides are usually anhedral and are present in accessory proportions (1 per cent or less) of the total rock mass. They appear either as microphenocrysts with grain sizes ranging up to 200 μm, inclusions in pyroxenes or as microcrystals in the groundmass. Patches of low-temperature mineral

alteration were identified only in thin sections from Whakapapaiti A (WPA) and Skyline Ridge (GR) flows (Fig. 3d).

BSE imaging on all samples from the Ruapehu lavas, shows that the Fe–Ti oxides exist either as homogeneous grains or as lamellar intergrowths of a highly reflective component and a less reflective component which we interpret as titanomagnetite ($Fe_{3-x}Ti_xO_4$) and ilmenite ($FeTiO_3$) or low Ti titanohematies ($Fe_{2-y}Ti_yO_3$) respectively, corresponding to oxidation indices 1–3 as defined by Watkins & Haggerty (1968). Within the visible range, the lamellae have a width of 4–10 μm and are either cross-hatched or parallel [e.g. samples from Whangaehu (WE) and Delta Corner (DC) flows, Figs 3e and f] and we suggest that they formed by progressive oxidation-exsolution caused by a shift in the equilibrium composition after formation of the primary mineral phases. WDX analysis conducted on isolated phenocrysts of titanomagnetite grains of the Ruapehu lavas reveals little compositional variability. The

Table 1. Holocene lava flows sampled from the Tongariro Volcanic Centre, descriptions, ages and palaeomagnetic directional data.

Flow	Age (ka)	Pmag age	Location		Pmag direction				Description
			Lat (°S)	Long (°E)	Dec (°)	Inc (°)	$\alpha95$ (°)	N	
Central Crater (CC)*	$<1.72 \pm 0.01^b$	200–500	39.133	175.655	20.8	−67.4	7.4	13	Basaltic a'a flow, sourced from Red Crater near the northern end of the TgVC. Individual blocks were sampled along the flow top surface.
Whangaehu (WE)	$<2.4^a$	2050–2400	39.292	175.650	359.5	−60.6	3.3	7	Massive end part of an andesitic lava flow with a blocky flow top. Samples were taken through the thickness of the flow (zones A–D).
Delta Corner (DC)	6 ± 2.4^a	7900–8200	39.255	175.561	8.5	−68.3	3.9	10	Ridge forming andesitic flow in Whakapapa ski field. Four sites were sampled in a section that exposes the flow's thickness, and across a lateral distance of ∼200 m (zones A–C).
Bruce Road (RP)	$5–10^b$	8500–8800	39.272	175.540	17.8	−60.8	4.0	7	A steep river gorge exposes a massive section through this andesitic flow. We present only the results from one site sampled from zone C (site RP02).
Taranaki Falls (TF)	8.8 ± 2.8^a	8900–9500 or 10 200-10 800	39.226	175.576	4.5	−49.5	3.2	16	Valley bottom flow, exposed along Wairere streambed. Three sites were sampled over a distance of several kilometres, from the out-washed flow interior (probably zone C).
Mangaturuturu (MT)	11.9 ± 2.2^a	> 10 500	39.291	175.522	8.7	−60.4	4.0	10	Andesitic flow, within a sequence of flows, exposed in a steep bluff. Hand samples and core samples were taken from the platey flow interior and directly surrounding rock (zone B).
Whakapapaiti A (WPA)	14.8 ± 3.0^a	N/A	39.253	175.530	358.1	−54.9	2.7	8	Ridge forming flow above a sequence of waterfalls. Cored samples were taken from three sites over a distance of c. 500 m, and additional hand samples from the platey flow interior (site WPA01) (zones B and C).
Skyline Ridge (GR)	15.1 ± 2.4^a	N/A	39.002	175.552	356.5	−81.4	3.8	11	Very exposed ridge top flow. Three sites were sampled over a distance of c. 1.5 km. Hand samples were taken from the platey flow interior (zones B and C).
Rangataua (RT)	$<15^c$	RT01	39.332	175.553	358.1	−65.4	3.8	3	Suite of andesitic lava flows covering an area of c. 40 km^2. The flow interior is exposed in a small number of stream cuts only, which were sampled at sites RT01, RT02 and RT03. Un-oriented hand samples were taken from the blocky flow top surface (Sites RT04 and RT05) (zone D). While all sites belong to the same package of flows, based on field evidence it cannot be established whether they belong to the same flow. The palaeomagnetic direction of site RT01 differs significantly from the mean direction of sites RT02 and RT03, suggesting a separation in time and that site RT01 may represent a different flow from the other two sites.
		RT02,3	39.333	175.537	10.7	−53.4	2.7	11	
		RT04	39.327	175.551	N/A	N/A	N/A	N/A	
		RT05	39.329	175.552	N/A	N/A	N/A	N/A	

Age (ka) based on a) ^{40}Ar/^{39}Ar dates (Conway et al., 2016), b) tephrochronology (Topping, 1974; Hobden, 1997; Lowe et al., 2013), c) morphology. Pmag Age: Refined palaeomagnetic emplacement ages (Greve et al, 2016) 3. Lat, Long are the latitude and longitude of the sampling location, respectively. Pmag direction: Palaeomagnetic direction: Dec = declination, Inc = inclination, N is total number of samples included in palaeodirection average. *CC flow: Direction calculated from four site mean directions.
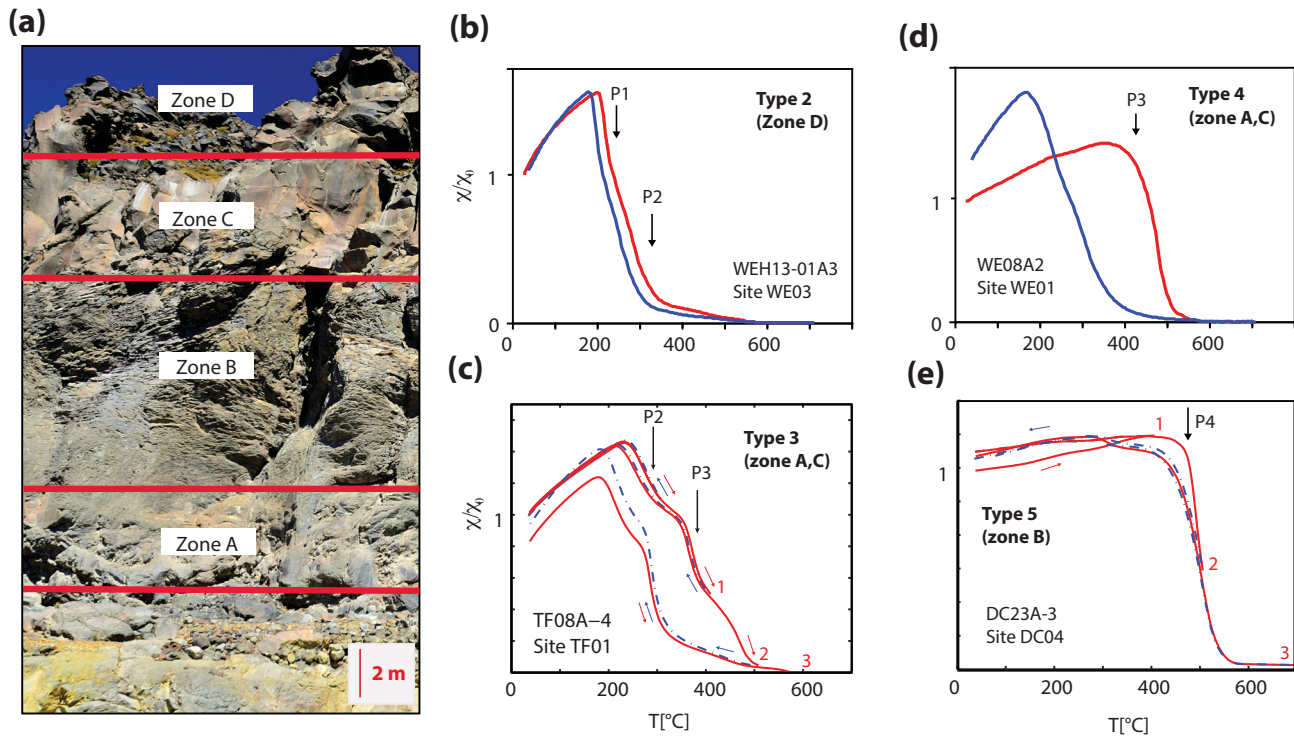
Figure 2. (a) Section through WE flow, illustrating the general zonation of flows. (b–e) Representative χ–T curves where red is the heating curve and blue the cooling curve. The approximate T_c's of compositional phases P1–P4 are shown. In (c) and (e) incremental heating curves, the endpoints of successive heating curves are numbered in red. In (c), the decay of compositional phases P2 and P3 into a composition with lower Curie temperature is clearly visible.

magnetite-ulvöspinel mixing factor x, calculated from the cation analyses following the procedures of Stormer (1983), ranges in value from 0.19 to 0.53 (19–53 per cent, Table 2).

3.3 Rock and thermomagnetic behaviour

The petrographic analyses described in Section 3.2 suggest that the magnetic minerals in samples from all sites and flows consist primarily of titanomagnetites or titanohematites/ilmenites with low to moderate oxidation states (indices 1 to 3 after Watkins & Haggerty 1968). The rock and thermomagnetic properties agree well with this observation (Greve *et al.* 2016). Fig. 4 shows the results of rock magnetic experiments. Isothermal remanent magnetization (IRM) acquisition and backfield coercivity of remanence curves of samples from all flows strongly resemble each other. The IRM curves saturate at applied fields below 250 mT and require backfields, B_{cr}, between 15 and 30 mT to demagnetize samples thereafter, as would be expected if the magnetic remanence is primarily carried by titanomagnetites of varying grainsize (Fig. 4a). Hysteresis loops of most samples show magnetic coercivities, B_c, between 5 and 15 mT (Fig. 4b): only samples from CC and Bruce Road (RP) flows yield higher coercivities, up to 30 mT (Fig. 4c). The ratios of saturation remanent magnetization (M_{rs}) to saturation magnetization (M_s) and coercivity of remanence (B_{cr}) to coercivity (B_c) fall into the range of values expected for PSD grains as defined by Day *et al.* (1977) and Dunlop (2002). However, based on the wide variation of grain sizes observed during mineral-optical analyses we suggest that these ratios are more likely to represent averages across spectra of coercivities.

Samples from each flow follow trends in M_{rs}/M_s versus B_c (Fig. 4c) and the coercivities measured on samples from WE flow

differ significantly with position in the flow: flow centre (zone B, site WE02) samples yield coercivities approximately twice as high as a sample from the flow top (zone D, site WE03). It is unlikely that the average composition of the remanence carriers differs throughout a flow, and it thus suggests that the samples from zone B have a smaller magnetic grain size. Differences between zones through the thickness of individual lava flows were also noted during the thermomagnetic experiments. Greve *et al.* (2016) distinguish between five different thermomagnetic curve types, which are summarized in Table 2 (see also Figs 2b–e). Type 1 behaviour is unique to samples from CC flow and shows increased mineral alteration on heating in an ambient atmosphere (M_s versus T experiments), as compared with heating experiments conducted in an inert, argon atmosphere (χ versus T experiments) (Table 2). In contrast, curve types 2 to 5, found in andesitic samples from Ruapehu, primarily differ in terms of their Curie temperature distribution and reversibility.

Each curve type indicates the presence of least one of four compositional phases identified in this study, similar to those also found in other studies of basic to intermediate composition lavas (e.g. Calvo *et al.* 2002; Biggin *et al.* 2007a): P1 ($150\,°C \leq T_c \leq 250\,°C$) appears only in the near-reversible type 2 curves which we found from flow top samples (zone D), such as those sampled at Rangataua (RT, all sites) and WE (site WE03) lava flows (Fig. 2b). In contrast, the intermediate T_c phases (P2: $250\,°C \leq T_c \leq 320\,°C$ and P3: $320\,°C \leq T_c \leq 450\,°C$) are observed in most samples but dominate in the irreversible type 3 and type 4 curves (Figs 2c and d), mostly obtained from samples from zones A and C (sites WE01, WE04, DC01–02, RP01–02, TF02–03, WPA02–03). Samples exhibiting type 3 or type 4 curves alter upon heating to temperatures higher than 400 °C, with a shift in T_c that is dependent on the peak temperature (Fig. 2c). Phase P4 dominates in the near reversible type 5 curves, typically abundant in samples from zone B (sites
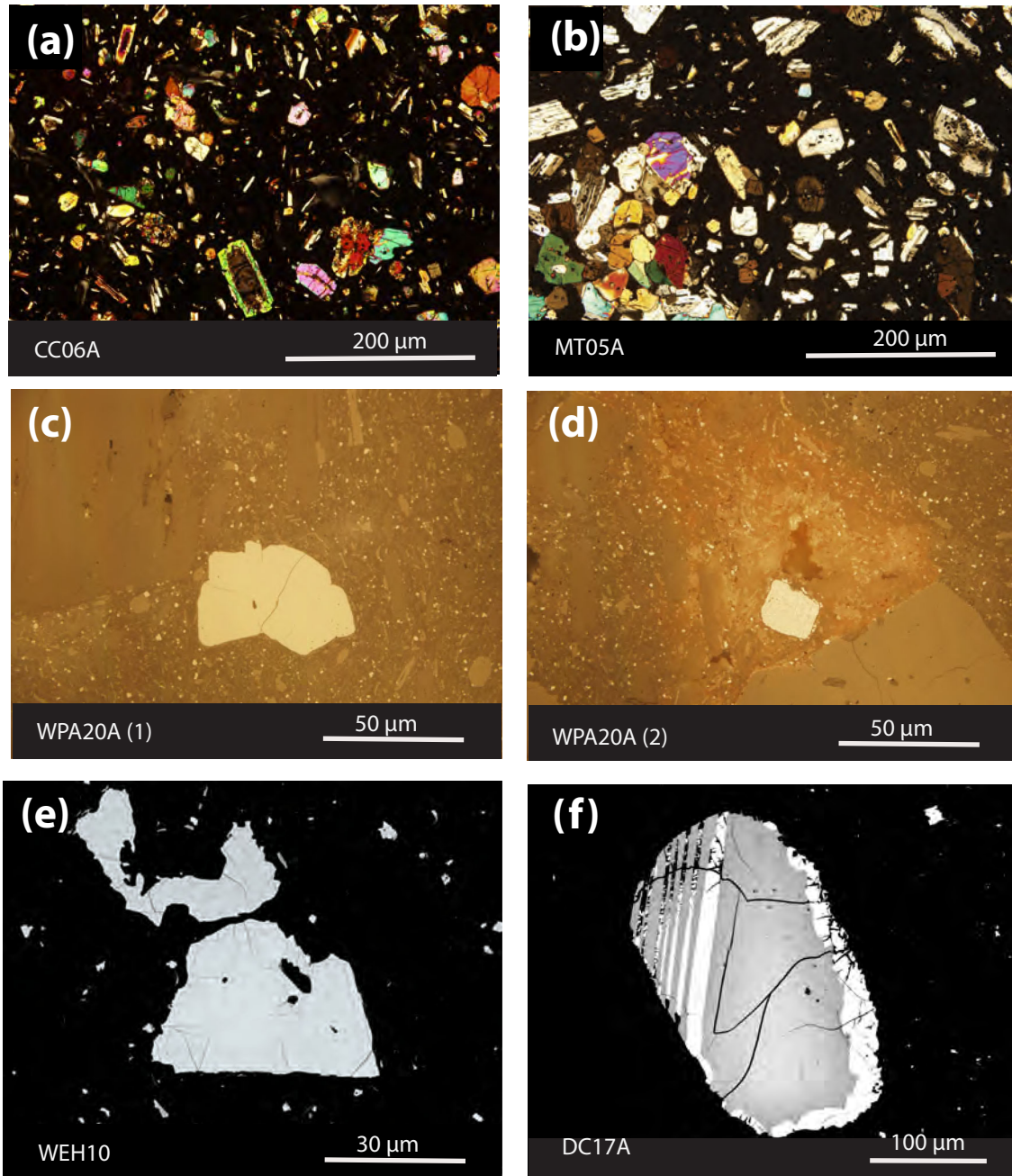
Figure 3. Representative photomicrographs from TgVC andesites. (a) Basaltic andesite from CC flow under cross-polarized transmitted light; (b) andesite from MT flow, transmitted light, cross-polarized (c) unaltered opaque (titanomagnetite) phenocryst under reflected light (WPA flow); (d) altered opaque (titanomagnetite) phenocryst (WPA) flow, reflected light. Patches of alteration can be identified by a discolouration along the grain boundaries of both the silicate and oxide phases. (e) Back-scattered electron (BSE) image of titanomagnetite with parallel and cross-hatched exsolution lamellae, (f) WE flow BSE image ilmenite grain, co-existing with titanomagnetite, DC flow.

WE02, DC03, MT01) (Fig. 2e). All five types of thermomagnetic curves are fully reversible if heating is stopped and the sample cooled from a temperature of 350 °C or less (Figs 2c and e). However, while samples with curve types 2, 3 and 4 (zones A, C, D) are dominated by compositional phases P1–P3 which have T_cs $\leq$ 450 °C and thus a significant part of their blocking temperature spectrum lies below 350 °C, samples from zone B (type 5 curves) are dominated by the high T_c phase P4. With the onset of thermochemical alteration at temperatures as low as 350 °C, below the major part of the blocking temperature spectrum of such samples, type 5 samples are thus less suitable for palaeointensity determination.

Quantitative analyses on titanomagnetite crystals from all Ruapehu flows give us a mixing factor, x between 0.19 and 0.53, which is compatible with the Curie temperatures of compositional phases P1, P2 and P3 (150 °C $\leq T_c \leq$ 450 °C, Lattard *et al.* (2006), Table 2). In contrast, in order to account for a $T_c > 500$ °C (phase P4) a near endmember composition, low Ti-titanomagnetite would be required ($x < 0.2$). This mixing factor is beyond the range of compositions identified during WDX analyses, suggesting the presence of low Ti-titanomagnetite phases with effective magnetic grain sizes that are smaller than the minimum resolution of the electron microprobe (<5 μm).

Table 2. Thermomagnetic curve characteristics and their occurrence on the zone within lava flows sampled. Also displayed are the ulvöspinel mixing coefficients x (in ranges) for synthetic titanomagnetites showing a similar T_c, and values calculated from wavelength dispersive analysis (WDX) on samples from the relevant zones in this study.

Type	Zone of flow	Characteristics	Titanomagnetite composition, x, from Curie temperature	x, from electron microprobe data
1	N/A	χ–T curves show one magnetic phase and little alteration, while M_s–T curves show an increase in T_c after heating, together with an increase in M_s after heating.	N/A	N/A
2 (Fig. 2b)	D	Characterised by multiple magnetic phases with different T_c's (P1: 150–250 °C, P4: > 500 °C). The curves are fully reversible.	P1: 0.45–0.66; P4 < 0.18	0.4–0.52
3 (Fig. 2c)	A, C	The heating curves show two or more phases with T_c's between 250 and 320 °C (P2) and between 320 and 450 °C (P3). The T_c's change after heating, the T_c shift is dependent on the peak temperature during an experiment.	P2: 0.4–0.45; P3: 0.2–0.4	0.33–0.53
4 (Fig. 2e)	A, C	Some curves have only one T_c upon heating (P4: > 500 °C), but two T_c's (P3, P4) during cooling.	P4 < 0.18	0.33–0.53
5 (Fig. 2d)	B	Characterized by a single phase of high T_c (P4), the heating and cooling curves are near reversible.	P4 < 0.18	0.19–0.53

Electron microprobe settings: accelerating voltage 15 kV, beam current 20 nA, beam width 1 μm; standards: $FeTiO_3$ for Ti-analyses, Fe_3O_4 for Fe elements probed for, analysis crystals: Ti (PeH) Mg, Si, Al (TAP), Fe (Lifl), Mn, Cr (Lifl). x calculated from Curie temperatures following Lattard *et al.* (2006). x calculated from electron microprobe data following Stormer (1983).
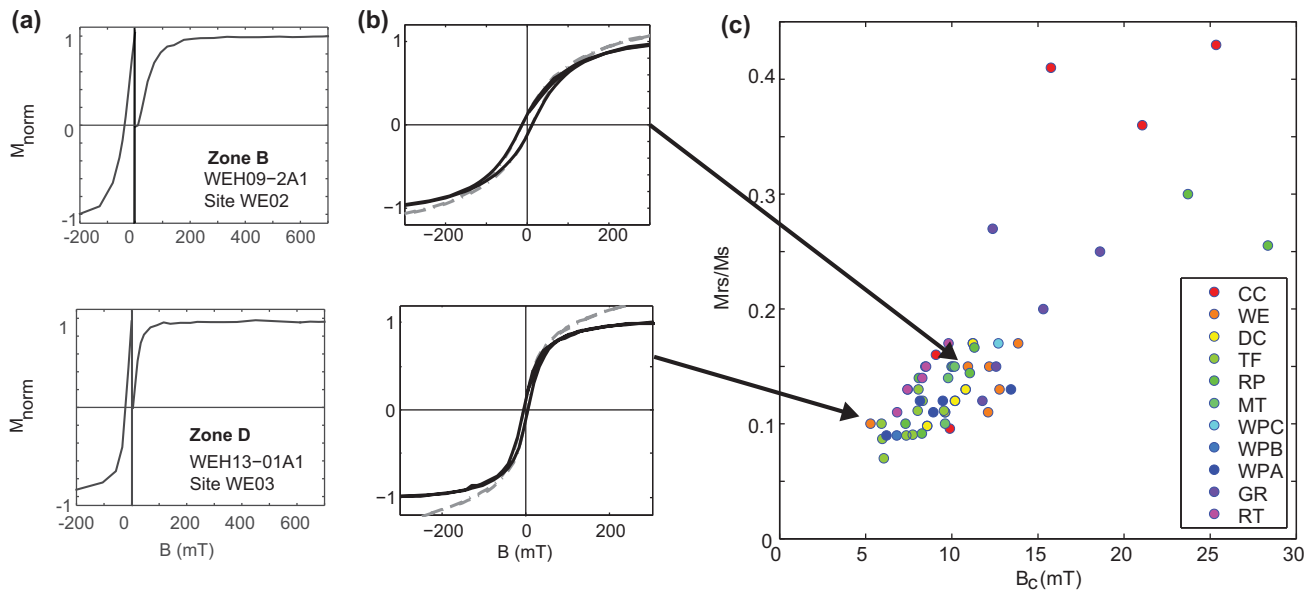

Figure 4. (a) Representative IRM and backfield curves and (b) corresponding hysteresis diagrams (normalized to saturation magnetization, M_s, after removal of the paramagnetic component) for samples taken from the top (zone D) and centre (zone B) of Whangaehu flow (WE). (c) The hysteresis properties of samples from all TgVC flows studied are displayed in a plot of M_{rs}/M_s against B_c.

We suggest that the presence of multiple compositional phases is the result of differing cooling rates throughout the andesitic flows sampled. The cooling, degassing and crystallization processes during and after emplacement of the lava flows may have caused a shift of the equilibrium composition within the spinel-orthorhombic system described by the Fe–Ti oxides (e.g. Sauerzapf *et al.* 2008). While quenching of the lava on the flow top preserved titanomagnetites close to their primary state (e.g. oxidation index 1 or 2, after Watkins & Haggerty 1968), cooling within the flow centre may have lasted up to weeks (Sigurdsson 2000). This would have allowed the titanomagnetites to undergo subsolidus exsolution, or the growth of sub-micron sized titanomagnetites within the rock matrix.

4 PALAEOINTENSITY

4.1 Methods

Up to ten standard sized specimens from each site were prepared for palaeointensity experimentation. Specimens were grouped according to their blocking temperature spectra, known from previous demagnetization experiments (Greve *et al.* 2016) and palaeointensity experiments were designed correspondingly. First palaeointensity experiments were carried out using the IZZI protocol (Tauxe & Staudigel 2004) and additional Coe-type (Coe 1967) experiments were conducted on specimens from sites that showed promising results during the first suite of experiments. Partial thermal remanent magnetization (pTRM) checks were carried out to monitor

alteration and additionally all thermal experiments were accompanied by low field susceptibility checks using a *Bartington* MS2 instrument in order to monitor mineral alteration. Furthermore, during Coe-type experiments we conducted a tail check (Riisager & Riisager 2001) following every second in-field step to monitor MD effects. Thermal palaeointensity experiments were carried out using either a *Magnetic Measurements Ltd* slow or fast cooling oven for thermal de- and remagnetization and measured using an *AGICO JR6* magnetometer at the University of Liverpool and an *AGICO JR6A* at Victoria University of Wellington. Prior to commencing the in-field steps, a profile of the total field strength along the oven was measured using a fluxgate magnetometer. The samples were placed within the most uniform (maximum field variation 1 per cent) space in the centre of the oven and each temperature was held for 30 min. The cooling times from temperatures between 300 and 600 °C to near room temperature were approximately 30 min in the fast cooling, and up to 2 hr in the slow cooling oven. A first suite of experiments was conducted using a laboratory field of 30 µT and later experiments in a field of 50 µT. Because the laboratory field could only be applied along the core-axis, the specimens were placed in the oven so that, alternating between specimens, the field was applied either parallel or antiparallel to the *z*-axis. Additionally, some palaeointensity experiments were aborted when the onset of thermal alteration became apparent from the susceptibility measurements.

Microwave palaeointensity experiments were carried out using the 14 GHz system at the University of Liverpool (see e.g. Stark *et al.* 2010). The technique uses ferromagnetic resonance (FMR) to excite the magnetic moments of the grains rather than heating the bulk sample but otherwise follows similar stepwise experimental procedures to the thermal experiments (Hill & Shaw 1999, 2000). For comparison, microwave experiments were carried out using similar protocols and, where possible, on specimens from the same samples as those used for thermal experiments. The field was always applied along the *z*-axis of the individual samples analogous to the thermal experiments. The sample size and positioning within the cavity varied slightly and the exact frequency (range 14.0–14.5 GHz) was fine-tuned prior to each experiment in order to achieve maximum absorption rates. The parameter affecting the demagnetization level is the total energy absorbed by a sample, which is a function of the power and exposure time of microwaves. Slight variation of the energy absorption can be caused by movement of a sample within the cavity and/or mineral alteration (Suttie *et al.* 2010). Repeatability of individual steps is a prerequisite for both Coe and IZZI protocols and differences were usually <3 per cent. We rejected or repeated steps where the absorption varied by more than 10 per cent from the first step at a given power level. The applied power was generally increased from a starting value of 10 W in steps between 2 and 5 W, with an exposure time of 5 s. If samples required further treatment after reaching 30 W the exposure time was increased in increments of 2 s. In contrast to the thermal experiments, microwave experiments were conducted on one specimen at a time, which enabled us to adjust the power increments according to the behaviour of the individual specimens. Prior to each intensity experiment we conducted a rapid demagnetization experiment on a test specimen from each sample to design suitable power steps and eliminate samples with strong overprinting.

All palaeointensity data in this study were analysed using *ThellierTool v4.22* (Leonhardt *et al.* 2004a). The software internal default criteria sets TTA and the less stringent TTB quantify the quality of the slope calculated from an Arai plot, pTRM and tail checks. We adopted these selection criteria but implemented small modifications as suggested by Paterson *et al.* (2014), here referred to as TTA* and TTB*:

(1) The zero-field remanence measurement should show straight line decay to the origin of a vector component (Zijderveld) plot. The anchored fit should make an angle, α, no larger than 15° with the free floating fit, and yield a maximum angular deviation (MAD_{anc}) smaller than 6° or 15° to pass TTA* and TTB*, respectively.

(2) Palaeointensity estimates should be calculated from at least five data points and include at least 35 per cent of the total NRM ($f \geq 0.35$) for both TTA* and TTB*.

(3) The quality of the slope fit in the Arai-diagram (β) is quantified using the standard error of the slope normalized by the absolute value of the slope. $\beta \leq 0.1$ to pass TTA* and $\beta \leq 0.15$ to pass TTB*. The quality factor, $q = fg\beta^{-1}$, should be ≥ 5 to pass TTA* and ≥ 0 to pass TTB*, where g is the gap factor of Coe *et al.* (1978).

(4) The maximum absolute difference produced by a pTRM check is calculated by vector subtraction and divided by the total TRM, $dCK \leq 7$ per cent and $dCK \leq 9$ per cent to pass TTA* and TTB*, respectively. The cumulative pTRM check failure ($dpal$) is quantified from the difference between the slope of an uncorrected palaeointensity estimate and the slope, corrected by the added effect of the alteration (see Valet *et al.* 1996), normalized by the uncorrected slope: $dpal = 100\frac{b-b*}{b}$ where b is the uncorrected and $b*$ the corrected slope. $dpal \leq 10$ per cent (TTA*), $dpal \leq 18$ per cent (TTB*).

(5) Tail checks (included as part of the Coe protocol) are quantified using the maximum difference between a zero-field measurement and a subsequent tail check, normalized by the NRM, $dTR \leq 10$ per cent (TTA*), 20 per cent (TTB*), and $dt*$, which accommodates the directional dependence of the pTRM tail (Leonhardt *et al.* 2004b), $dt* \leq 9$ per cent (TTA*), $dt* \leq 99$ per cent (TTB*).

Palaeointensities were calculated from the best-fitting slope within the Arai plot. Table 3 lists all succesful palaeointensity results, the statistical parameters and, for later discussion, distinguishes between results that meet TTA* and TTB* selection criteria. In two cases (WEH13–01A, CC38–1) we included the result of a microwave experiment that narrowly failed the pTRM check criteria due to differences in the power absorption within the microwave cavity between the check and original step (e.g. Fig. 5a). We also include the results from two specimens (MT13A-3 and RP14A-3) that slightly fail the *f*-criterion, but where the palaeointensities fall into the range of all other succesful results from the same flow. For later discussion we also list all data for which a palaeointensity estimate could be made, but which do not strictly meet the selection criteria and that are thus not included in the site or flow means calculated. We consider each specimen from which an acceptable result has been obtained to yield an independent record of palaeointensity, and so to calculate site and flow mean results we average results from the individual specimens. At WE flow, we observed systematic differences between the palaeointensity estimates from flow-top and flow-centre samples. We list both mean values, as well as an overall mean, calculated as the mid-point of the total range defined by flow-top and flow-centre average palaeointensities with their respective standard deviations, and an uncertainty that encompasses the two extremes, as has been suggested and proven suitable in experimental studies of historical lavas by Biggin *et al.* (2007a).

4.2 Palaeointensity results

Palaeointensity estimates were obtained from six of the ten lava flows studied: CC, WE, RT, Taranaki Falls (TF), RP and MT. A

Table 3. Palaeointensity results by specimen and site means. The uppermost two rows define the TTA* and TTB* criteria sets used. These are based on the TTA and TTB criteria sets of Leonhardt *et al.* (2004a), and include modifications suggested by Paterson *et al.* (2014). We include (in italics) palaeointensity results that did not meet the selection criteria and were therefore not included in the calculation of site and flow means.

Site (Zone)	ID	Type	B_{lab}	Prot	Interval	N	f	β	q	MAD (°)	α (°)	dCK (%)	dpal (%)	dTR (%)	dt* (%)	Int (μT)	σ	Sel/(N/n)
						≥ 5	≥ 0.35	≤0.1	≥ 5	≤ 6	≤ 15	≤ 7	≤ 10	≤ 10	≤ 9			A*
						≥ 5	≥ 0.35	≤ 0.15	≥ 0	≤ 15	≤ 15	≤ 9	≤ 18	≤ 20	≤ 99			B*
CC02	CC12A-1	M	50	IZZI	0–40 Ws	5	0.49	0.03	13.2	1.3	2.5	1.5	8.53			71.4	1.8	A*
CC02	CC12A-2	M	50	Coe	0–60 Ws	9	0.98	0.01	80.4	0.8	0.6	1.0	0.55	2.6	2.7	78.6	0.8	A*
CC02	*CC13B*	*T*	*50*	*Coe*	*0–325 °C*	*6*	*0.87*	*0.02*	*44.7*	*1.5*	*1.2*	*16.0*	*23.5*	*2.3*	*3.5*	*69.6*	*1.0*	
CC02	CC13C	T	50	Coe	0–300 °C	5	0.92	0.01	62.1	1.1	0.4	6.0	2.85	0.5	0.0	67.9	0.6	A*
CC02	*CC14B*	*T*	*50*	*Coe*	*0–325 °C*	*6*	*0.8*	*0.02*	*40.5*	*1.6*	*1.8*	*11.6*	*19.6*	*0.5*	*0*	*69.9*	*1.0*	
CC03	CC22A-1	M	50	Coe	25–155 Ws	6	0.7	0.01	42.3	0.8	1.5	7.3	17.6	6.5	5.7	64.9	0.8	B*
CC04	*CC28B*	*T*	*50*	*Coe*	*200–350 °C*	*4*	*0.4*	*0.02*	*8.9*	*0.7*	*0.3*	*1.1*	*4.2*	*3.4*	*0*	*56.8*	*1.4*	
CC05	*CC35–4*	*M*	*50*	*IZZI*	*75–360 °C*	*11*	*0.9*	*0.04*	*20.6*	*1.0*	*0.1*	*9.1*	*27.6*			*52.0*	*1.9*	
CC05	CC36–1	M	50	IZZI	0–120 Ws	5	1.0	0.03	18.2	1.7	1.4	8.3	9.0			75.0	2.0	B*
CC05	*CC36–2*	*M*	*50*	*Coe*	*100–120 Ws*	*4*	*0.5*	*0.02*	*9.8*	*1.3*	*1.4*	*4.6*	*11.0*	*2.4*	*9.6*	*84.3*	*2.8*	
CC05	CC38–1*	M	50	Coe	0–210 Ws	9	0.57	0.05	8.8	1.1	3.0	1.9	0.89	1.9	35.9	75.5	4.1	
CC06	CC45A-2	M	50	IZZI	0–70 Ws	9	0.9	0.03	22.9	8.2	9.1	5.1	17.9			71.6	2.3	B*
MEAN																**72.1**	**4.7**	**7/13**
Mean including specimens that pass TTA only*																*72.6*	*5.5*	*3/13*
WE02 (B)	WEH10–2C-5	M	50	IZZI	0–140 Ws	9	0.55	0.11	4.2	3.3	9.5	3.3	7.17			62.1	6.7	B*
WE04 (C)	WE16A-3	M	50	IZZI	125–280Ws	6	0.35	0.05	5.1	0.6	0.9	5.7	9.0			60.7	2.8	A*
WE04 (C)	WE16A-4	M	50	Coe	50–288 Ws	10	0.75	0.04	15.9	0.4	4.0	5.0	11.3	4.1	2.6	67.8	2.7	B*
WE04 (C)	*WE17B*	*T*	*50*	*Coe*	*0–350 °C*	*4*	*0.29*	*0.04*	*4.2*	*0.9*	*0.6*	*0.5*	*2.1*	*0.6*	*0*	*62.5*	*2.7*	
WE04 (C)	*WE20A-4*	*M*	*50*	*Coe*	*0–185 Ws*	*12*	*0.81*	*0.02*	*32.9*	*1.6*	*2.6*	*7.1*	*24.6*	*0*	*0*	*65.2*	*1.4*	
Mean zone A–C																**63.5**	**3.8**	**3/13**
WE03 (D)	*WEH13–1A-3*	*M*	*50*	*IZZI*	*65–105 Ws*	*5*	*0.62*	*0.06*	*8.0*	*3.0*	*2.6*	*3.7*	*13.2*	*0*	*0*	*51.7*	*2.9*	
WE03 (D)	WEH13–01A-4*	M	50	Coe	0–120 Ws	7	0.89	0.03	19.6	3.4	1.9	10.8	13.29	2.6	0.7	54.4	1.8	
WE03 (D)	WEH13–10C	T	50	Coe	100–350 °C	8	0.71	0.03	17.1	2.1	3.3	2.4	1.1	1.8	0	54.9	1.7	A*
Mean zone D																**54.7**	**0.4**	**2/3**
*Mean including all data***																*60.8*	*6.5***	
RP02 (C)	RP14A-3	M	30	IZZI	50–112.5 Ws	6	0.32	0.03	8.9	0.8	1.7	2.6	9.92			51.2	1.5	
RP02 (C)	RP14B	T	30	Coe	0–425 °C	8	0.49	0.05	7.5	1.3	3.1	2.6	5.03	4.2	5.2	48.4	2.6	A*
RP02 (C)	RP14C	T	30	IZZI	0–325 °C	6	0.44	0.06	5.9	1.5	2.8	2.8	5.5			57.1	3.2	A*
RP02 (C)	RP15A	T	30	Coe	0–400 °C	7	0.44	0.04	10.3	0.7	0.5	6.4	7.73	1.4	0.0	51.2	1.8	A*
RP02 (C)	RP15B	T	30	Coe	0–400 °C	7	0.51	0.06	6.6	1.0	2.3	5.5	6.93	4.0	4.0	48.7	3.1	A*
RP02 (C)	*RP15C-2*	*M*	*30*	*Coe*	*25–100 Ws*	*5*	*0.37*	*0.02*	*4.2*	*2.2*	*3.6*	*6.8*	*34.1*	*2.5*	*0*	*52.1*	*3.1*	
RP02 (C)	RP16A-3	M	30	IZZI	37.5–100 Ws	6	0.36	0.03	8.4	1.3	2.9	2.0	10.18			48.9	1.6	B*
RP02 (C)	*RP16A-4*	*M*	*30*	*Coe*	*40–115 Ws*	*6*	*0.4*	*0.04*	*7.5*	*1.1*	*2.0*	*4.5*	*26.9*	*0.4*	*3.0*	*49.9*	*2.1*	
RP02 (C)	RP16B	T	30	IZZI	100–325 °C	5	0.41	0.03	10.9	0.7	0.8	1.3	9.40			57.8	1.5	A*
RP02 (C)	RP18B	T	30	Coe	0–350 °C	6	0.57	0.02	23.1	0.7	0.9	1.8	2.30	0.6	0.0	53.5	1.1	A*
RP02 (C)	RP19C	T	30	IZZI	0–400 °C	9	0.52	0.10	4.5	1.4	3.2	8.9	28.50			50.1	4.7	B*
MEAN																**51.9**	**3.5**	**9/11**
Mean, including specimens that pass TTA only*																*52.8*	*4.1*	*6/11*
TF01 (B)	*TF06B*	*T*	*30*	*IZZI*	*100–550 Ws*	*13*	*1.0*	*0.09*	*10.1*	*2.0*	*2.5*	*6.03*	*27.4*			*32.2*	*2.8*	
TF01 (B)	*TF09C*	*T*	*30*	*IZZI*	*100–400Ws*	*8*	*0.6*	*0.05*	*8.8*	*1.1*	*0.9*	*7.1*	*37.1*			*34.8*	*1.9*	
TF02 (C)	TF11B	T	30	IZZI	0–300 °C	5	0.49	0.11	3.2	1.3	2.2	1.7	1.50			41.3	4.6	B*
TF02 (C)	TF11C	T	30	Coe	0–425 °C	10	0.6	0.09	5.7	1.2	0.8	1.6	6.70	4.7	5.36	34.7	3.0	A*
TF02 (C)	TF12A-2	M	30	IZZI	25–105 Ws	8	0.52	0.05	9.1	3.0	7.2	1.4	9.15			31.6	1.5	A*
TF02 (C)	TF13B	T	30	Coe	0–425 °C	10	0.58	0.06	8.2	1.8	2.1	3.2	3.26	1.2	0	33.8	2.0	A*
TF02 (C)	TF16B	T	30	IZZI	0–300 °C	5	0.54	0.03	15.3	1.6	2.5	3.4	10.36			41.0	1.0	B*
TF03 (C)	TF19B	T	30	IZZI	0–300 °C	5	0.43	0.11	2.8	1.1	1.0	0.7	0.29			49.6	5.5	B*
TF03 (C)	*TF20C*	*T*	*30*	*IZZI*	*200–425 °C*	*8*	*0.39*	*0.12*	*2.8*	*1.6*	*3.3*	*35.4*	*87.2*			*29.3*	*3.4*	
TF03 (C)	TF21B	T	30	Coe	0–425 °C	10	0.52	0.07	6.2	1.7	4.7	3.9	8.36	2.5	3.23	37.1	2.4	A*
TF03 (C)	TF22C	T	30	Coe	0–425 °C	10	0.75	0.06	10.5	1.4	2.4	4.6	4.04	0.6	0	36.9	2.1	A*
MEAN																**38.3**	**5.7**	**8/16**
Mean including specimens that pass TTA only*																*34.8*	*2.3*	*5/16*
MT01 (B)	MT13A-3	M	50	IZZI	20–80 Ws	6	0.32	0.03	7.8	0.8	0.6	0.4	0.06			42.9	1.3	
MT01 (B)	*MT13A-4*	*M*	*50*	*IZZI*	*25–100 Ws*	*16*	*0.78*	*0.3*	*0.8*	*1.9*	*2.5*	*7.0*	*68.7*			*32.5*	*10.4*	
MT01 (B)	MTH14–1A-2	M	50	IZZI	65–224 Ws	8	0.87	0.04	15.9	2.8	2.5	3.8	7.40			32.3	1.3	A*
MT01 (B)	MT14A-3	M	50	Coe	75–217 Ws	8	0.6	0.08	6.0	2.7	5.9	8.9	8.5	8.4	10.3	36.9	2.9	B*
MT01 (B)	MTH03–1A-1	M	50	Coe	50–150 Ws	5	0.65	0.09	4.8	2.0	4.4	3.5	6.69	3.3	12.8	34.8	3.0	B*
MT01 (B)	MTH03–1A-2	M	50	IZZI	25–125 Ws	5	0.58	0.03	13.5	5.1	7.6	5.7	0.18			40.8	1.3	A*
MT01 (B)	MTH02–2A-2	M	50	IZZI	25–125 Ws	6	0.45	0.03	8.1	2.8	4.8	0.5	2.20			42.6	3.5	B*
MT01 (B)	MTH02–2C	T	50	IZZI	0–400 °C	11	0.70	0.07	9.3	1.8	3.3	4.9	4.32			36.9	2.4	A*
MT01 (B)	MTH02–4C	T	50	IZZI	0–400 °C	11	0.65	0.06	9.0	1.2	2.2	3.9	1.04			37.7	2.4	A*
MT01 (B)	MTH02–3C	T	50	Coe	100–350 °C	6	0.5	0.04	8.4	1.2	1.5	3.0	6.7	2.3	0	43.7	2.0	A*
MT01 (B)	MTH02–4B	T	50	Coe	0–350 °C	6	0.64	0.05	9.5	1.9	2.3	2.0	3.27	4.6	3.52	44.1	2.3	A*
MEAN																**39.3**	**4.1**	**10/17**
Mean including specimens that pass TTA only*																*39.3*	*4.5*	*6/17*
RT01 (D)	RT3A-2	M	50	IZZI	0–54 Ws	5	0.45	0.1	2.8	3.4	1.6	0.4	0.59			36.1	3.8	B*
RT01 (D)	*RT3A-5*	*M*	*50*	*Coe*	*35–90 Ws*	*6*	*0.77*	*0.05*	*11.5*	*1.8*	*2.3*	*2.3*	*1.3*	*12.6*	*18.9*	*19.9*	*1.0*	
RT01 (D)	RT4A-1	M	50	Coe	20–60 Ws	5	0.59	0.02	26.8	2.3	3.9	0.5	1.04	2.1	2.55	25.4	0.4	A*
RT01 (D)	RT4A-2	M	50	IZZI	45–150 Ws	8	0.49	0.07	6.0	3.0	5.5	2.3	4.33			37.7	2.6	A*

Table 3 – (*Continued.*)

Site (Zone)	ID	Type	B_{lab}	Prot	Interval	N	f	β	q	MAD (°)	α (°)	dCK (%)	dpal (%)	dTR (%)	dt* (%)	Int (μT)	σ	Sel/(N/n)
						≥ 5	≥ 0.35	≤0.1	≥ 5	≤ 6	≤ 15	≤ 7	≤ 10	≤ 10	≤ 9			A*
						≥ 5	≥ 0.35	≤ 0.15	> 0	≤ 15	≤ 15	≤ 9	≤ 18	≤ 20	≤ 99			B*
MEAN Site RT01																**33.1**	**6.7**	**3/5**
RT04 (D)	RT25H-5B	T	50	IZZI	150–325 °C	8	0.84	0.03	26.7	2.8	2.3	4.2	0.97			26.7	0.7	A*
RT04 (D)	RT25H-6B	T	50	IZZI	150–325 °C	8	0.84	0.02	35.0	3.9	3.7	2.4	0.31			26.4	0.5	A*
RT04 (D)	RT25H-4A-5	M	50	Coe	50–90 Ws	5	0.49	0.04	7.9	5.3	6.8	2.8	4.30	4.8	9.54	31.9	1.3	B*
MEAN site RT04																**28.3**	**3.1**	**3/3**
RT05 (D)	RT27H-1C	T	50	IZZI	100–375 °C	11	0.82	0.03	22.0	2.9	4.4	2.7	3.44			33.6	1.1	A*
RT05 (D)	RT27H-2C	T	50	IZZI	150–275 °C	6	0.6	0.12	3.9	1.9	3.1	2.3	3.4			34.8	4.1	B*
RT05 (D)	RT27H-1A-2	M	50	IZZI	0–70 Ws	5	0.82	0.04	15.8	3.2	2.8	1.3	2.93			38.6	1.4	A*
MEAN Site RT05																**35.7**	**2.6**	**3/4**
Overall mean sites RT01, 04, 05																**32.4**	**5.1**	**9/15**
Mean including specimens that pass TTA* only																***32.1***	***5.8***	***7/15***

Notes. ID corresponds to the specimen ID (Sampling naming convention: XX-zzN-n for cored samples, XXzzH-iiN-n, for hand samples, where XX is the unit, zz is the core-number, N denotes the specimen ID, A being the outermost specimen of a core, another number 'n' was added when individual specimens were subdivided into multiple specimens for microwave experiments). Type: M = microwave palaeointensity, T = thermal palaeointensity. B_{lab} is the laboratory field used. Prot. is the experimental protocol used. Interval is the temperature interval selected from thermal experiments in °C or the minimum and maximum steps selected of the energy applied during microwave experiments in Ws. N, f, β, q, MAD, dCK, dpal, dTR, dt* are statistical parameters calculated following the standardized palaeointensity definitions (Paterson *et al.* 2014). MAD is the maximum angular deviation of the pca fit when anchored to the origin. Int is the palaeointensity with one standard deviation uncertainty (σ). Sel. = selection criteria used. A* = TTA*, B* = TTB* as discussed in the text. Averaging: (N/n) (number of successful specimen-results included in average/total number of experiments carried out).

*pTRM or tail check failure associated with inconsistencies in the energy absorbed during microwave treatment. These data were included in flow mean calculations.

**The best overall estimate of the mean palaeointensity for Whangaehu Flow (WE) is calculated as the mid-point of the total range defined by the flow-top and flow-centre average palaeointensities with their respective standard deviations, with an overall uncertainty that encompasses the two extremes.

total of 19 palaeointensity experiments were also conducted on samples from WPA, GR and DC flows despite these flows showing evidence of significant overprinting during demagnetization experiments (Greve *et al.* 2016) and/or signs of low-temperature alteration during the optical investigations. Other than one experiment on a sample from DC flow, there were no successful palaeointensity results obtained from these three flows and they will not be further discussed. Specimens from sites RT02 and RT03 yield strong overprints and inconsistent palaeointensity results and were excluded from further analysis as well.

For the six flows that did yield successful palaeointensity results, 44 out of a total of 88 palaeointensity experiments met either the TTA* or TTB* selection criteria. Representative successful results are displayed in Figs 5(a)–(e), and a rejected result is shown in Fig 5(f). Some specimens carried minor viscous components that were usually removed during the early demagnetization steps (Fig. 5). Common reasons for rejection of results were non-linearity of the Arai plot, non-repeatability of in-field steps (pTRM checks) at early demagnetization levels or tail-check failure. Both check failures were often associated with a systematic deviation of the demagnetization trajectory from the origin of the vector component plot (Fig. 5f). In most cases mineral alteration and associated failure of pTRM checks was accompanied by a change in the slope of the Arai plots and all affected data points were rigorously excluded from the calculation of a palaeointensity (Figs 5c–e). In all thermal experiments the pTRM checks failed at temperatures above c. 350 °C (Fig. 5d).

Fig. 6 illustrates the variability of individual results compared with the corresponding flow mean. All but two results fall within 20 per cent of the mean and there are no systematic differences between the results from microwave and thermal experiments. At WE flow, results obtained from one site that belongs to the flow top zone D (site WE03) yield a palaeointensity estimate that is 14 per cent lower than the ones obtained from samples from the flow interior zones B and C (sites WE02 and WE04). The number of palaeointensity results that pass the selection criteria is insuffi-

cient to draw firm conclusions regarding the effect of differences in the positioning of sampling sites within lava flows. However as a precautionary approach, we provide an error estimate that encompasses both extremes (see Section 4.1) to accommodate potential systematic differences within the palaeointensity dataset. The five RT sites sampled belong to the same eruptive package (Conway *et al.* 2016), however based on the field relations it is unclear whether the sites RT01, RT04 and RT05 belong to flow units of similar age or not (Table 1, Fig. 1) and additionally only un-oriented samples were obtained from RT04 and RT05 so no directional information can be derived. The palaeointensity results from sites RT01, RT04 and RT05 are indistinguishable at the 2σ level, and thus the data have been combined to give one flow average (Tables 3 and 4).

5 DISCUSSION

5.1 Data quality and success rates

The new flow mean palaeointensities presented here have standard deviations of 5.7 μT or less (Table 4). This degree of uncertainty compares well with other palaeointensity studies on Holocene lavas (e.g. Tanaka *et al.* 1994, 2009; Stanton *et al.* 2011; Di Chiara *et al.* 2014). For TF flow the dispersion could be reduced by applying more stringent selection criteria (TTA*, Fig. 6, Table 3). The palaeointensity results that pass criteria set TTA* fall into the range of the mean calculated for all flows meeting selection criteria TTB*, however with a smaller number of successful data a discrimination against TTB*-type data may result in placing too high confidence on individual results or the removal of useful data (Biggin *et al.* 2003, 2007a; Paterson *et al.* 2014). This becomes particularly evident on flows such as WE, RP, TF and MT, where rejected results support the experiments that pass the selection criteria (Table 3).

Fig. 7 displays the overall success rates of palaeointensity experiments in relation to the zone within the lava flows sampled and compared with the different methods used. On average, the thermal
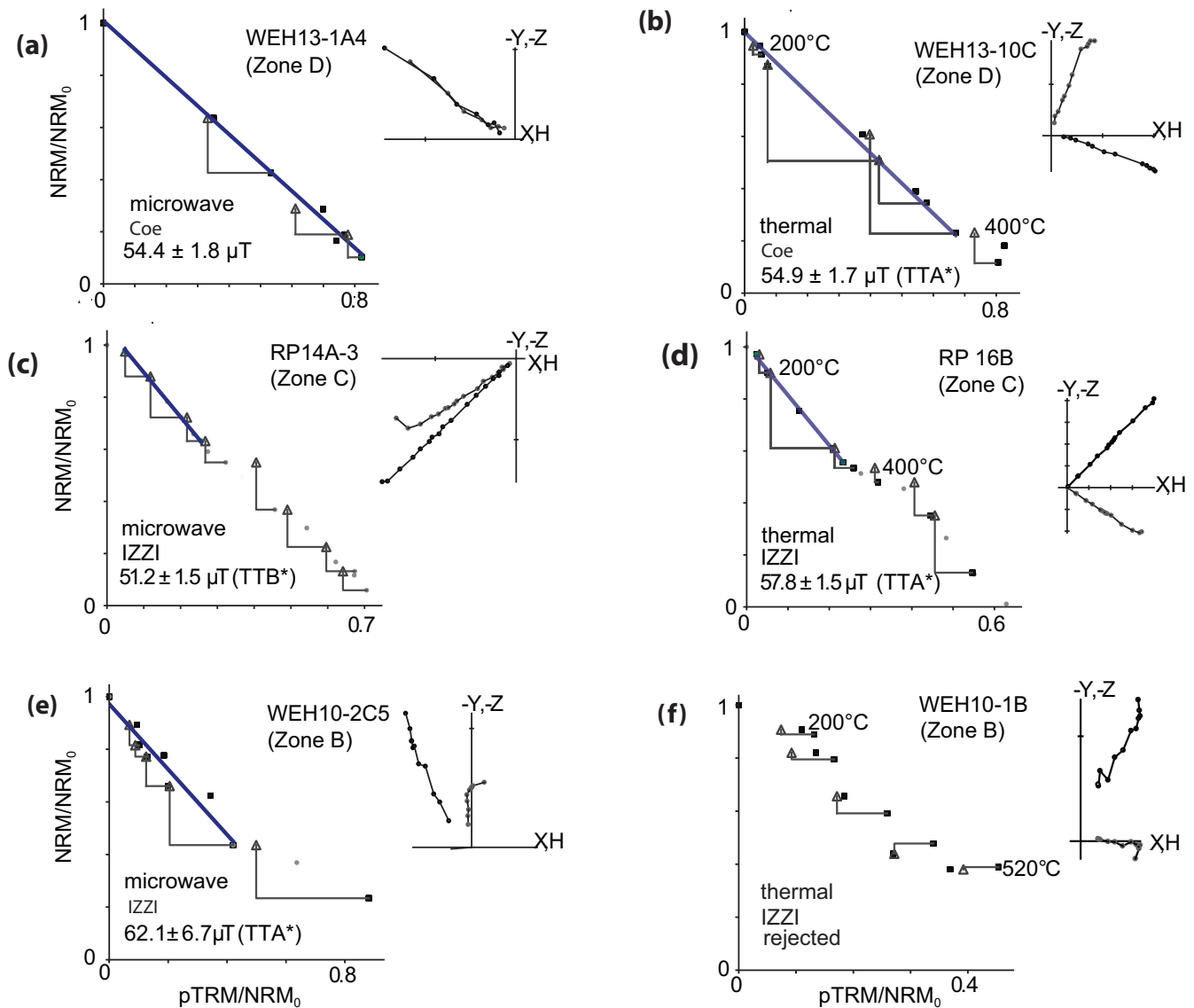
Figure 5. Representative Arai and Zijderveld plots (insets) for microwave (left) and thermal (right) palaeointensity experiments, ordered by zone within the thickness of lava flows. (a) Although specimen WE13–1A4 did not meet either TTA* or TTB* selection criteria, it was included in the calculation of a site mean, since failure could be attributed to non-repeatability of the microwave absorption during the second pTRM check. (b–e) Successful experiments, (f) a rejected result. Figures produced using ThellierGUI (Shaar & Tauxe 2013).

experiments showed higher success rates than microwave experiments (Fig. 7a), which we attribute to failure of pTRM checks or zigzagging caused by inconsistencies between the power absorption in the microwave cavity during repeated treatment steps. During future studies, such failure may be mitigated by using protocols that do not require repeated treatment steps, such as the quasi-perpendicular method (Biggin *et al.* 2007b). IZZI protocols appear to lead to slightly higher success rates and higher quality data than Coe-type protocols (Fig. 7b). We suggest that the addition of tail checks may enhance oxy-exsolution of the titanium oxides during Coe-type experiments, causing cumulative pTRM check failure at earlier demagnetization levels.

The overall success rates, as well as the quality of the Arai plots, pTRM and tail checks differ with the location through the vertical thickness of the lava flows, and with associated differences in the rock and thermomagnetic properties. In all thermal experiments the pTRM checks failed at temperatures above c. 350 °C, which corresponds to the onset temperature of thermochemical alteration

observed in the repeated measurement of χ versus T experiments (Figs 2c and e). During microwave experiments, the pTRM checks predominantly failed at corresponding demagnetization levels (Figs 5c and e). It is therefore not surprising that the highest overall success rates and the largest number of experiments meeting the more stringent selection criteria TTA* were recorded from samples from zones C and D, where the presence of grains with blocking temperatures ≤350 °C (Table 2) allowed demagnetization of a significant proportion of the remanence prior to the onset of thermal alteration. In contrast, experiments on specimens from the flow centre (zone B) did not usually meet the pTRM-check requirements and in some cases the tail checks failed also (Table 3). Zone D was sampled at RT and WE flows only. Due to the lower blocking temperature and coercivity distribution of samples from this zone, viscous overprints affected a significant proportion of the remanence. This resulted in the rejection of all data from sites RT02 and RT03 and samples from zone D thus yield on average lower success rates than samples from zone C.
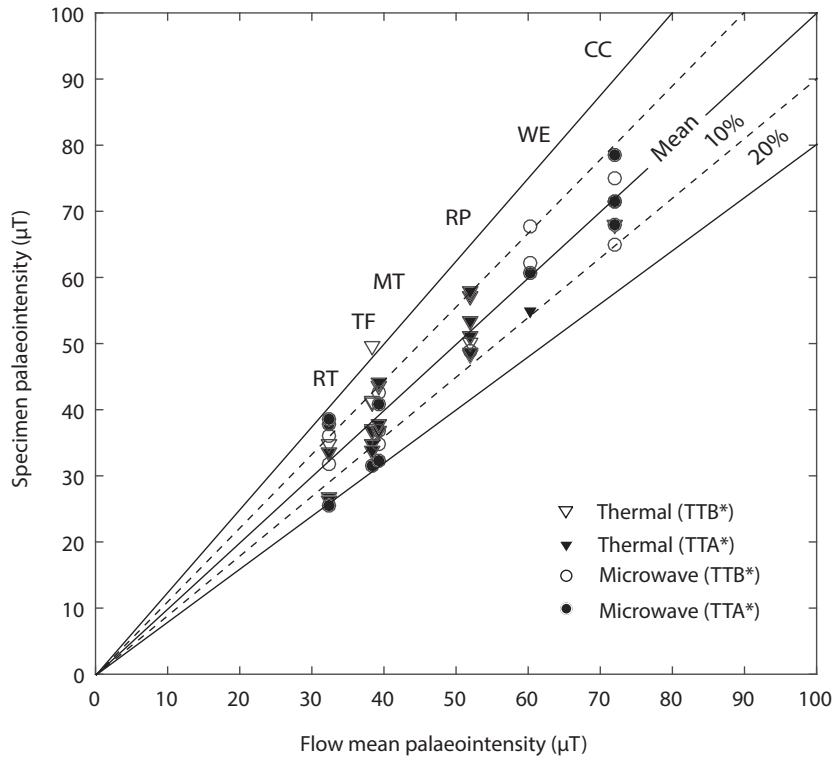
Figure 6. Distribution of all successful palaeointensity data about the best flow mean palaeointensity, distinguishing between the results that pass the more stringent TTA* (closed symbols) and the less stringent TTB* (open symbols) selection criteria and experiments that were conducted using the thermal (triangles) and microwave methods (circles). Also shown are the limits at which the palaeointensity differs by 10 per cent or 20 per cent of the best flow mean.

Table 4. Summary of the flow mean palaeointensities, virtual dipole moments and axial dipole moments.

Flow	Age (pmag) yr BP	Age (ind) yr BP	Dec (°)	Inc (°)	α_{95} (°)	$N_{\rm d}$	Int $\pm \sigma$ (μT)	$N_{\rm p}/N_{\rm t}$	VDM (10^{22} Am^2)	VADM (10^{22} Am^2)
CC*	300 ± 200	1718 ± 0.01	20.8	− 67.4	7.4	13	72.1 ± 4.7	7/13	11.2 ± 1.4	12.6 ± 0.8
WE*	2225 ± 175	200 ± 2200	359.5	− 60.6	3.3	7	60.8 ± 6.5	5/16	10.3 ± 1.4	10.6 ± 1.1
RP	8650 ± 150	7500 ± 2500	17.8	− 60.8	4.0	7	51.9 ± 3.5	9/11	8.8 ± 0.9	9.0 ± 0.6
TF	9200 ± 300 or 10 500 ± 300	8800 ± 2800	4.5	− 49.5	3.2	16	38.3 ± 5.7	8/16	7.5 ± 1.3	6.7 ± 1.0
MT	>10 500	11 900 ± 2200	8.7	− 60.4	4	10	39.3 ± 4.1	10/17	6.7 ± 0.9	6.8 ± 0.7
RT01	>10 800	<15 000	358.1	− 65.4	3.8	1	32.4 ± 5.1	9/15	5.2 ± 1.0	5.6 ± 0.9

Note. Age (pmag) and Age (ind), palaeomagnetic and independent ages after Greve *et al.* (2016). Dec, declination; Inc, inclination; α_{95}, semi-angle of cone of 95 per cent confidence in mean direction; $N_{\rm d}$, total number of samples included in palaeodirection average,; Int, flow mean palaeointensity; $N_{\rm p}/N_{\rm t}$, number of successful palaeointensity experiments/total number of experiments; VDM, virtual dipole moment; VADM, virtual axial dipole moment. *CC flow: direction calculated from four site mean directions. WE flow: palaeointensity estimate calculated as the mid-point of the total range defined by the flow-top and flow-centre average palaeointensities with their respective standard deviations, with an overall uncertainty that encompasses the two extremes.

Systematic differences between palaeointensity results obtained from units of the same age, potential sources for data scatter and difficulties during palaeointensity experiments have been described widely and the cause is often due to variations in the rock magnetic behaviour (e.g. Hill & Shaw 2000; Boehnel *et al.* 2003; Yamamoto *et al.* 2003; Biggin *et al.* 2007a; De Groot *et al.* 2014; Monster *et al.* 2015). While the wide sampling campaign presented in this study allows correlation of the rock magnetic results obtained at different flows, the limited number of palaeointensity results that pass the selection criteria makes it difficult to directly link differences between individual palaeointensity results to rock magnetic properties or the positions of samples within flows. The differences observed between flow top and flow centre samples at WE, for instance, are close to the data dispersion observed on all other flows, suggesting that specific rock magnetic contributions often remain undetected. We suggest that at WE flow these differences are linked

to variations in the oxy-exsolution state and inherent grain size of the remanence carriers throughout the flow as indicated by the thermomagnetic curves (Fig. 2). Cooling rate may also be a contributing factor, however experimental studies have shown that it is negligible for remanence carriers that show on average PSD or MD sized properties (Yu 2011; Biggin *et al.* 2013; Ferk *et al.* 2014).

In contrast, the similarity between the behaviour of samples during palaeointensity experiments conducted on sister samples using microwave and thermal methods in this study of samples from Mt Ruapehu flows is remarkable. The compatibility of microwave and thermal palaeointensity studies has been demonstrated sufficiently in the past (e.g. Hill *et al.* 2002; Stanton *et al.* 2011). The fact that the pTRM checks fail at similar levels of demagnetization for both microwave and thermal experiments, suggests that in this case the microwave system was in fact acting as a mini thermal demagnetizer (e.g. Suttie *et al.* 2010).
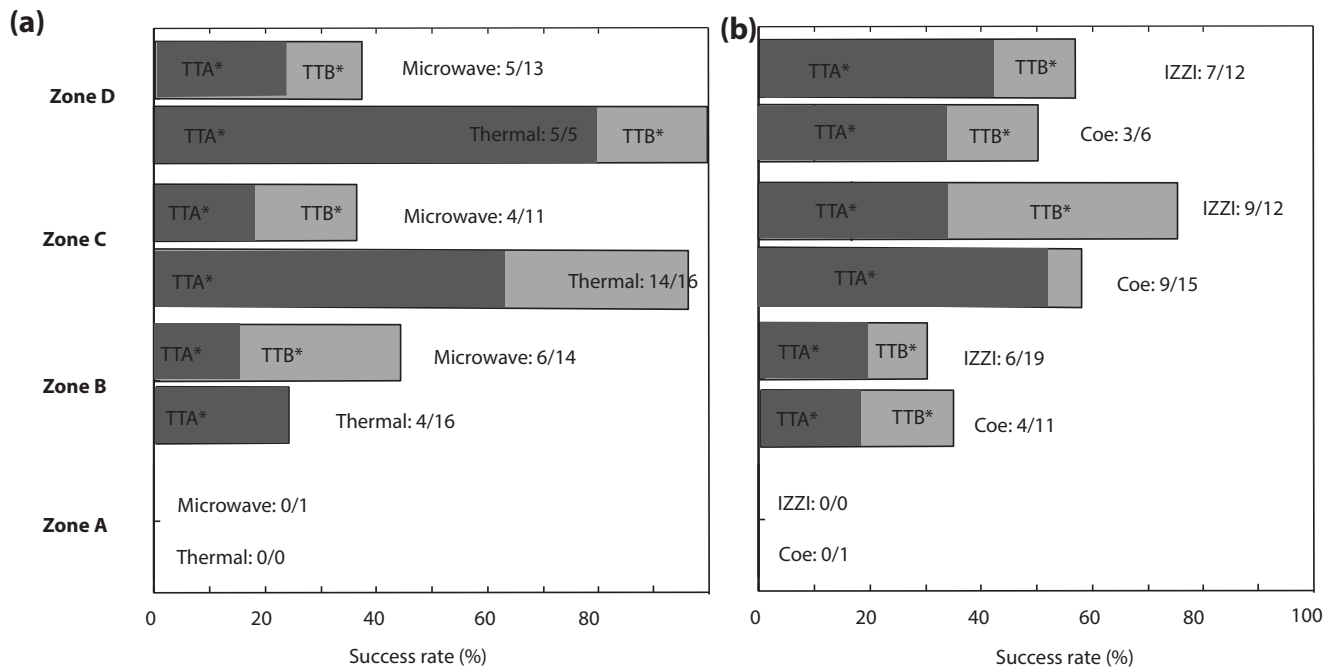
Figure 7. Percentage of successful experiments versus total number of experiments carried out on samples from different zones within the flows studied using (a) the microwave and thermal palaeointensity methods, (b) IZZI and Coe-type protocols. We also distinguish between experiments that pass the more stringent TTA* and the less stringent TTB* selection criteria and display the total number of experiments that meet either selection criteria as a percentage of the total number of experiments conducted. Excluded are data from Skyline Ridge (GR), Whakapapaiti A (WPA), Delta Corner (DC) flows and sites RT02 and RT03. Zone D is the brecciated flow top, zone C is the blocky interior, zone B is the platey flow centre and zone A is the flow base (Table 2, Fig. 2a).

5.2 Comparison with existing datasets and global field models

Table 4 is a summary of our best flow mean palaeointensities together with the age control and palaeomagnetic directions described by Greve *et al.* (2016), and calculated virtual dipole moments (VDMs) and virtual axial dipole moments (VADMs). Figs 8(a)–(c) display the palaeodirectional results of Greve *et al.* (2016), and the new palaeointensity data of this study with both their independent radiometric age constraints (Conway *et al.* 2016) and their palaeomagnetic age constraints, superimposed on the continuous PSV record from Lake Mavora, Southland, New Zealand (Turner *et al.* 2015), and the predictions of two recently published global field models, pfm9k.1b (Nilsson *et al.* 2014) and SHA.DIF.14k (Pavón-Carrasco *et al.* 2014). The Lake Mavora record is the only continuous PSV record from the region published to date. The intensity record is one of relative palaeointensity, and we apply the calibration factor suggested by Turner *et al.* (2015), which is based on the earliest absolute intensity recordings from New Zealand. The SHA.DIF.14k model is based exclusively on volcanic and archaeomagnetic data from the GEOMAGIA50v2 database (Donadini *et al.* 2006; Korhonen *et al.* 2008). The pfm9k.1b model, on the other hand is also constrained by sedimentary data. The inclusion of sedimentary data significantly enhances the regional data support but generally also leads to smoother models, mainly due to the large dating uncertainties of sedimentary records (e.g. Nilsson *et al.* 2014). For compatibility, the model predictions were calculated at 39.2°S, 175.54°E and the Lake Mavora Curve was relocated to the same coordinates using a virtual geocentric dipole (VGP) transformation/inverse transformation process (Noel & Batt 1990). In Fig. 8(d) we display the VADMs calculated from the flow mean palaeointensities, in comparison to the global VADM reconstruction of Knudsen *et al.* (2008). For a more comprehensive discussion

including all palaeomagnetic data from New Zealand the reader is referred to Greve & Turner (2017).

The new TgVC palaeointensity data show an overall trend from lower to higher palaeointensities through the Holocene. The pre-9 ka lavas, including MT, TF and RT flows yield below average intensities of 39.3 ± 4.1, 38.3 ± 5.7 and 32.4 ± 5.1 μT, respectively, while the younger flows return intensities of 51.9 ± 3.5 μT (RP), 60.8 ± 6.5 μT (WE) and 72.1 ± 4.7 μT (CC).

Significant differences are visible, particularly between 6000 and 3000 yr BP, between the SHA.DIF.14k and pfm9k.1b intensity predictions and the Lake Mavora intensity record (which was not included in the construction of either model). The comparison highlights the challenges involved in reconstructing geomagnetic field variations in the southern hemisphere with models based on the limited palaeomagnetic data available from the region, and emphasizes the importance of including new palaeomagnetic records, such as those reported here, in the next generation of models. Furthermore, improvements of the radiocarbon-based age control of earlier volcanic datasets from New Zealand, which are included in the current models has resulted in revisions of up to 900 yr (Greve & Turner 2017).

Despite these uncertainties, both models and the Lake Mavora record all describe a similar broad trend from lower to higher palaeointensity through the Holocene, in agreement with our new data. Since the palaeomagnetically refined ages of Greve *et al.* (2016) were determined by matching only the palaeodirections of each unit, we can here use the intensity data to test the validity of these ages. We note that the highest palaeointensity, that of the CC flow, correlates with the peak intensity of model pfm9k.1b, which supports its young palaeomagnetic age of 300 ± 200 yr BP. When the palaeomagnetic ages of Greve *et al.* (2016) are adopted (red circles and uncertainty bars on Fig. 8c), we also note that the new data generally agree with the Lake Mavora record as well as the
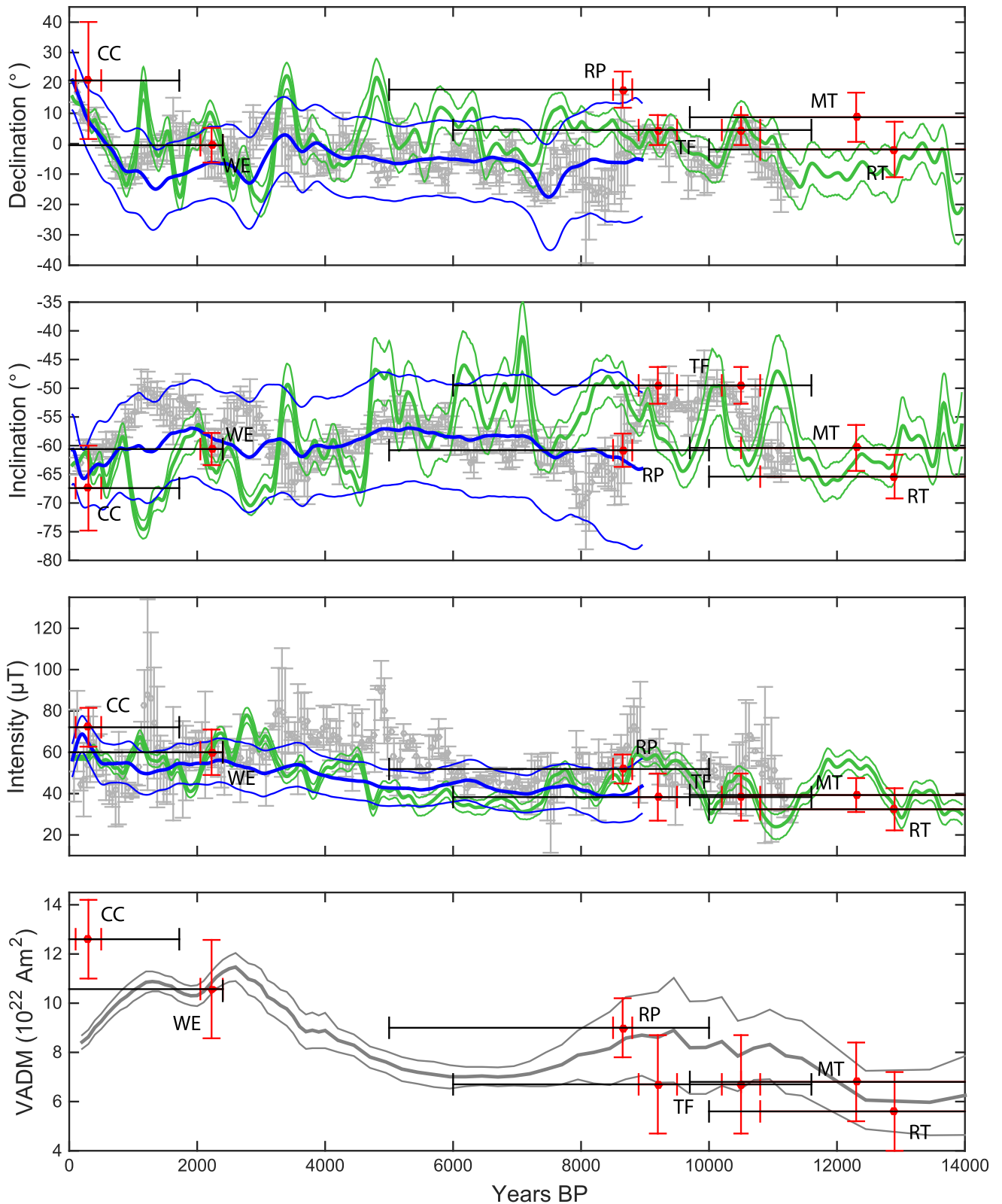
Figure 8. Discrete declination (a), inclination (b) and palaeointensity (c) records of this study showing both the independent (black lines) and palaeomagnetic age (red) constraints, superimposed on the continuous sediment record from Lake Mavora (Turner *et al.* 2015) (grey), and global field models pfm9k.1b (Nilsson *et al.* 2014) (blue) and SHA.DIF.14 K (Pavón-Carrasco *et al.* 2014) (green). The models were calculated at 39.2°S, 175.54°E. The Lake Mavora relative palaeointensity record was scaled to historical absolute measurements, as suggested by Turner *et al.* (2015), and both directions and intensities were relocated to 39.2°S, 175.54°E, using VGP/inverse transformation calculations. (d) VADMs calculated for each flow compared with the global VADM reconstruction of Knudsen *et al.* (2008) (grey). All data and model predictions are shown with 95 per cent confidence bounds.

geomagnetic field model predictions, particularly if the older possible palaeomagnetic age, of 10 500 $\pm$ 300 yr BP is adopted for flow TF.

With the exception of CC flow, the VADMs calculated from our new palaeointensity data fit within or close to the bounds of the global average VADM reconstruction of Knudsen *et al.* (2008) (Fig. 8d). The high palaeointensity, and VADM of 12.6 $\pm$ 0.8 $\times$ 10^{22} Am^2, of CC flow however contrasts markedly with the rapid decrease in the VADM over the past 1500 yr shown in the global reconstruction, and in historical data for the past 400 yr, culminating in the present day value of 7.72 $\times$ 10^{22} Am^2 (Thébault *et al.* 2015). Observational data for the last few centuries (Jackson *et al.* 2000), Turner *et al.*'s (2015) Lake Mavora record and CC's easterly declination and steep inclination (Dec. = 20.8°, Inc. = −67.4°) all suggest anomalously high flux beneath the SW Pacific region over the last few centuries and are thus in support of this palaeointensity estimate.

6 CONCLUSIONS

We report and discuss the results of a detailed palaeointensity study conducted on Holocene lava flows of intermediate composition from the Tongariro Volcanic Centre, New Zealand. The suitability of the samples and their primary remanence for palaeointensity studies was tested using a combination of rock magnetic experiments and mineral-optical investigations. Both thermal Thellier-type and microwave experimental procedures were then employed for the determination of palaeointensities. New palaeointensity estimates were successfully obtained from six of the ten flows studied, with values ranging between 32.4 $\pm$ 5.1 and 72.1 $\pm$ 4.7 µT.

The new absolute intensity data presented here, together with the palaeodirections of Greve *et al.* (2016), will be important to help constrain global field models which currently suffer a paucity of absolute palaeosecular variation data from the southern hemisphere. The data will also aid in the calibration of relative palaeointensity curves obtained from sediments from the region.

The palaeointensities describe a similar overall trend from lower to higher palaeointensities throughout the Holocene to that calculated from global field models pfm9k.1b (Nilsson *et al.* 2014) and SHA.DIF.14k (Pavón-Carrasco *et al.* 2014) and that described by global axial dipole moment compilations (Knudsen *et al.* 2008) for the early Holocene. In the late Holocene, the high palaeointensity estimate of CC flow (300 $\pm$ 200 yr BP) supports the development of high magnetic flux beneath the SW Pacific region.

The new data correlate well with the palaeosecular variation swings of the scaled relative palaeointensity curve from the sediments of Lake Mavora, New Zealand (Turner *et al.* 2015). This further supports the palaeomagnetic age estimates by Greve *et al.* (2016), which were based on correlation of directional data only.

Finally, the detailed sampling allows us to draw conclusions regarding the suitability for palaeointensity studies of samples from different locations within the vertical thickness of lava flows. Significant differences are seen between the rock magnetic properties and behaviour during palaeointensity experiments of samples from different zones within flows. Samples from the platey-fractured flow-centres yield, on average, higher Curie and blocking temperatures and lower coercivities than samples from the flow tops. We suggest that this outcome is related to differences in the oxidation and exsolution states of the titanomagnetites in the samples, in relation to differing cooling times. Success rates and palaeointensity

results are related to the location within the vertical thickness of a flow sampled. Highest success rates are found in locations between flow tops and flow centres, where a significant proportion of the magnetic remanence is carried by grains with blocking temperatures between 200 °C and 350 °C; lowest success rates were observed on samples from the flow centres.

REFERENCES

Biggin, A., Boehnel, H. & Zuniga, F., 2003. How many palaeointensity determinations are required from a single lava flow to constitute a reliable average?, *Geophys. Res. Lett.,* **30**(11), 1575, doi:10.1029/2003GL017146.

Biggin, A.J., Perrin, M. & Dekkers, M.J., 2007a. A reliable absolute palaeointensity determination obtained from a non-ideal recorder, *Earth planet. Sci. Lett.,* **257**(3), 545–563.

Biggin, A.J., Perrin, M. & Shaw, J., 2007b. A comparison of a quasi-perpendicular method of absolute palaeointensity determination with other thermal and microwave techniques, *Earth planet. Sci. Lett.,* **257**, 564–581.

Biggin, A.J., Badejo, S., Hodgson, E., Muxworthy, A.R., Shaw, J. & Dekkers, M.J., 2013. The effect of cooling rate on the intensity of thermoremanent magnetization (TRM) acquired by assemblages of pseudo-single domain, multidomain and interacting single-domain grains, *Geophys. J. Int.,* **193**, 1239–1249.

Boehnel, H., Biggin, A.J., Walton, D., Shaw, J. & Share, J.A., 2003. Microwave palaeointensities from a recent Mexican lava flow, baked sediments and reheated pottery, *Earth planet. Sci. Lett.,* **214**, 221–236.

Calvo, M., Prévot, M., Perrin, M. & Riisager, J., 2002. Investigating the reasons for the failure of palaeointensity experiments: a study on historical lava flows from Mt. Etna (Italy), *Geophys. J. Int.,* **149**, 44–63.

Coe, R.S., 1967. Paleo-intensities of the Earth's magnetic field determined from Tertiary and Quaternary rocks, *J. geophys. Res.,* **72**(12), 3247–3262.

Coe, R.S., Grommé, S. & Mankinen, E.A., 1978. Geomagnetic paleointensities from radiocarbon-dated lava flows on Hawaii and the question of the pacific nondipole low, *J. geophys. Res.,* **83**(B4), 1740–1756.

Constable, C., Korte, M. & Panovska, S., 2016. Persistent high paleosecular variation activity in southern hemisphere for at least 10 000 years, *Earth planet. Sci. Lett.,* **453**, 78–86.

Conway, C., Leonard, G.S., Townsend, D.B., Calvert, A.T., Wilson, C.J.N., Gamble, J.A. & Eaves, S.R., 2016. A high-resolution ^{40}Ar/^{39}Ar lava chronology and edifice construction history for Ruapehu volcano, New Zealand, *J. Volcanol. Geotherm. Res.,* **32**, 152–179.

Day, R., Fuller, M. & Schmidt, A., 1977. Hysteresis properties of titanomagnetites: grain-size and compositional dependence, *Phys. Earth planet. Inter.,* **13**, 260–267.

De Groot, L.V.D., Dekkers, M.J., Visscher, M. & Maat, G.W., 2014. Magnetic properties and paleointensities as function of depth in a Hawaiian lava flow, *Geochem. Geophys. Geosyst.,* **15**(4), 1096–1112.

Di Chiara, F., Tauxe, L. & Sperana, F., 2014. Paleointensity determination from São Miguel (Azores Archipelago) over the last 3 ka, *Phys. Earth planet. Inter.,* **234,** 1–13.

Donadini, F., Korhonen, K., Riisager, P. & Pesonen, L., 2006. Database for holocene geomagnetic intensity information, *EOS, Trans. Am. geophys. Un.,* **87,** 137–143.

Dunlop, D.J., 2002. Theory and application of the Day plot (M_{rs}/M_s versus H_{cr}/H_c) 1. Theoretical curves and tests using titanomagnetite data, *J. geophys. Res.,* **107**(B3), EPM 4-1–EPM 4-22.

Dunlop, D. & Özdemir, O., 1997. *Rock Magnetism: Fundamental and Frontiers,* Cambridge Univ. Press.

Eaves, S.R. *et al.*, 2015. A test of the cosmogenic He^3 production rate in the south-west Pacific (39°S), *J. Quat. Sci.,* **30,** 79–87.

Ferk, A., Leonhardt, R., Hess, K.-U., Koch, S., Egli, R., Krasa, D. & Dingwell, D.B., 2014. Influence of cooling rate on thermoremanence of magnetite grains: identifying the role of different magnetic domain states, *J. geophys. Res.,* **119**(3), 1599–1606.

Gamble, J.A., Price, R.C., Smith, I.E.M., McIntosh, W.C. & Dunbar, N.W., 2003. ^{40}Ar/^{39}Ar geochronology of magmatic activity, magma flux and hazards at Ruapehu volcano, Taupo Volcanic Zone, New Zealand, *J. Volcanol. Geotherm. Res.,* **120**(3), 271–287.

Greve, A. & Turner, G.M., 2017. New and revised palaeomagnetic secular variation (PSV) records from postglacial volcanic materials in New Zealand, *Phys. Earth planet. Inter.,* **269,** 1–17.

Greve, A., Turner, G.M., Conway, C.E., Townsend, D.B., Gamble, J.A. & Leonard, G.S., 2016. Palaeomagnetic refinement of the eruption ages of Holocene lava flows, and implications for the eruptive history of the Tongariro Volcanic Centre, New Zealand, *Geophys. J. Int.,* **207**(2), 702–718.

Hill, M.J. & Shaw, J., 1999. Palaeointensity results for historic lavas from Mt Etna using microwave demagnetization/remagnetization in a modified Thellier-type experiment, *Geophys. J. Int.,* **139**, 583–590.

Hill, M.J. & Shaw, J., 2000. Magnetic field intensity study of the 1960 Kilauea lava flow, Hawaii, using the microwave palaeointensity technique, *Geophys. J. Int.,* **142,** 487–504.

Hill, M.J., Gratton, M.N. & Shaw, J., 2002. A comparison of thermal and microwave palaeomagnetic techniques using lava containing laboratory induced remanence, *Geophys. J. Int.,* **151**(1), 157–163.

Hobden, B.J., 1997. Modelling magmatic trends in time and space, eruptive and magmatic history of Tongariro Volcanic Complex, *PhD thesis*, University of Canterbury, New Zealand.

Hobden, B., Houghton, B., Lanphere, M. & Nairn, I., 1996. Growth of the Tongariro volcanic complex: New evidence from K-Ar age determinations, *N.Z. J. Geol. Geophys.,* **39**(1), 151–154.

Hobden, B., Houghton, B. & Nairn, I., 2002. Growth of a young, frequently active composite cone: Ngauruhoe volcano, New Zealand, *Bull. Volcanol.,* **64,** 392–409.

Jackson, A., Jonkers, A.R. & Walker, M.R., 2000. Four centuries of geomagnetic secular variation from historical records, *Phil. Trans. R. Soc. A*, **358**(1768), 957–990.

Knudsen, M.F., Riisager, P., Donadini, F., Snowball, I., Muscheler, R., Korhonen, K. & Pesonen, L.J., 2008. Variations in the geomagnetic dipole moment during the Holocene and the past 50 kyr, *Earth planet. Sci. Lett.,* **272,** 319–329.

Koenigsberger, J.G., 1938. Natural residual magnetism of eruptive rocks, *J. geophys. Res.,* **43**(3), 299–320.

Korhonen, K., Donadini, F., Riisager, P. & Pesonen, L.J., 2008. GEOMAGIA50: an archeointensity database with PHP and MySQL, *Geochem. Geophys. Geosyst.,* **9,** 1–14.

Lattard, D., Engelmann, R., Kotny, A. & Sauerzapf, U., 2006. Curie temperatures of synthetic titanomagnetites in the Fe-Ti-O system: Effects of composition, crystal chemistry, and thermomagnetic methods, *J. geophys. Res.,* **111,** B12S28, doi:10.1029/2006JB004591.

Leonhardt, R., Heunemann, C. & Krasa, D., 2004a. Analyzing absolute paleointensity determinations: acceptance criteria and the software ThellierTool4.0, *Geochem. Geophys. Geosyst.,* **5,** Q12016, doi:10.1029/2004GC000807.

Leonhardt, R., Krasa, D. & Coe, R.S., 2004b. Multidomain behavior during Thellier paleointensity experiments: a phenomenological model, *Phys. Earth planet. Inter.,* **147**(2–3), 127–140.

Levi, S., 1977. The effect of magnetite particle size on paleointensity determinations of the geomagnetic field, *Phys. Earth planet. Inter.,* **13,** 245–259.

Lowe, D.J., Blaauw, M., Hogg, A.G. & Newnham, R.M., 2013. Ages of 24 widespread tephras erupted since 30,000 years ago in New Zealand, with re-evaluation of the timing and palaeoclimatic implications of the Lateglacial cool episode recorded at Kaipo bog, *Quat. Sci. Rev.,* **74,** 170–194.

Monster, M.W.L., de Groot, L.V., Biggin, A.J. & Dekkers, M.J., 2015. The performance of various palaeointensity techniques as a function of rock magnetic behaviour – a case study for La Palma, *Phys. Earth planet. Inter.,* **242,** 36–49.

Nilsson, A., Holme, R., Korte, M., Suttie, N. & Hill, M., 2014. Reconstructing Holocene geomagnetic field variation: new methods, models and implications, *Geophys. J. Int.,* **198,** 229–248.

Noel, M. & Batt, C.M., 1990. A method for correcting geographically separated remanence directions for the purpose of archaeomagnetic dating, *Geophys. J. Int.,* **102,** 753–756.

Olson, P., 2002. The disappearing dipole, *Nature,* **416,** 591–594.

Paterson, G.A., Tauxe, L., Biggin, A.J., Shaar, R. & Jonestrask, L.C., 2014. On improving the selection of Thellier-type paleointensity data, *Geochem. Geophys. Geosyst.,* **15**(4), 1180–1192.

Pavón-Carrasco, F.J., Osete, M.L., Torta, J.M. & De Santis, A., 2014. A geomagnetic field model for the Holocene based on archaeomagnetic and lava flow data, *Earth planet. Sci. Lett.,* **388,** 98–109.

Price, R.C., Gamble, J.A., Smith, I.E.M., Maas, R., Waight, T., Stewart, R.B. & Woodhead, J., 2012. The anatomy of an andesite volcano: a time-stratigraphic study of andesite petrogenesis and crustal evolution at Ruapehu Volcano, New Zealand, *J. Petrol.,* **53,** 2139–2189.

Riisager, P. & Riisager, J., 2001. Detecting multidomain magnetic grains in Thellier palaeointensity experiments, *Phys. Earth planet. Inter.,* **125,** 111–117.

Sauerzapf, U., Lattard, D., Burchard, M. & Engelmann, R., 2008. The Titanomagnetite-Ilmenite Equilibrium: new experimental data and thermo-oxybarometric application to the crystallization of basic to intermediate rocks, *J. Petrol.,* **49,** 1161–1185.

Selkin, A. & Tauxe, L., 2000. Long-term variations in palaeointensity, *Phil. Trans. R. Soc. A,* **358,** 1065–1088.

Shaar, R. & Tauxe, L., 2013. Thellier GUI: an integrated tool for analyzing paleointensity data from Thellier-type experiments, *Geochem. Geophys. Geosyst.,* **14**(3), 677–692.

Sigurdsson, H., 2000. *Encyclopedia of Volcanoes,* Academic Press.

Stanton, T., Riisager, P., Knudsen, M.F. & Thordarson, T., 2011. New palaeointensity data from Holocene Icelandic lavas, *Phys. Earth planet. Inter.,* **186,** 1–10.

Stark, F., Cassidy, J., Hill, M., Shaw, J. & Sheppard, P., 2010. Establishing a first archaeointensity record for the SW Pacific, *Earth planet. Sci. Lett.,* **198,** 113–124.

Stormer, J.C., 1983. The effects of recalculation on estimates of temperature and oxygen fugacity from analyses of multicomponent iron-titanium oxides, *Am. Mineral.,* **68,** 586–594.

Suttie, N., Shaw, J. & Hill, M.J., 2010. Direct demonstration of microwave demagnetization of a whole rock sample with minimal heating, *Earth planet. Sci. Lett.,* **292**(3–4), 357–362.

Tanaka, H., Otsuka, A., Tachibana, T. & Kono, M., 1994. Paleointensities for 10–22 ka from volcanic rocks in Japan and New Zealand, *Earth planet. Sci. Lett.,* **122**(1–2), 29–42.

Tanaka, H., Komuro, N. & Turner, G.M., 2009. Palaeosecular variation for 0.1–21 ka from the Okataina Volcanic Centre, New Zealand, *Earth Planets Space,* **61**(1), 213–225.

Tauxe, L. & Staudigel, H., 2004. Strength of the geomagnetic field in the cretaceous normal superchron: new data from submarine basaltic glass of the Troodos Ophiolite, *Geochem. Geophys. Geosyst.,* **5,** Q02H06, doi:10.1029/2003GC000635.

Thébault, E. *et al.*, 2015. International geomagnetic reference field: the 12th generation, *Earth Planets Space,* **67,** 79, doi:10.1186/s40623-015-0228-9.

Thellier, E. & Thellier, O., 1959. Sur l'intensité du champ magnétique terrestre dans le passé historique et géologique, *Ann. Geophys.,* **15,** 285–376.

Topping, W.W., 1974. Some aspects of quaternary history of Tongariro Volcanic Centre, unpublished *PhD thesis*, Victoria University of Wellington.

Tost, M. & Cronin, S.J., 2015. Linking distal volcaniclastic sedimentation and stratigraphy with the development of Ruapehu volcano, New Zealand, *Bull. Volcanol.,* **77**(11), 1–17.

Turner, G.M., Howarth, J.D., de Gelder, G.I.N.O. & Fitzsimons, S.J., 2015. A new high-resolution record of Holocene geomagnetic secular variation from New Zealand, *Earth planet. Sci. Lett.,* **430**, 296–307.

Valet, J.-P., Brassart, J., Meur, I.L., Soler, V., Quidelleur, X., Tric, E. & Gillot, P.Y., 1996. Absolute paleointensity and magnetomineralogical changes, *J. geophys. Res.,* **101**(B11), 25 029–25 044.

Watkins, N.D. & Haggerty, S.E., 1968. Oxidation and magnetic polarity in single icelandic lavas and dikes, *Geophys. J. Int.,* **15,** 305–315.

Yamamoto, Y., Tsunakawa, H. & Shibuya, H., 2003. Palaeointensity study of the Hawaiian 1960 lava: implications for possible causes of erroneously high intensities, *Geophys. J. Int.,* **153**, 263–276.

Yu, Y., 2011. Importance of cooling rate dependence of thermoremanence in paleointensity determination, *J. geophys. Res.,* **116,** 1–8.